Design and Modeling of an Active Aeroelastic Wing

Gregory W. Reich

Bachelor of Aerospace Engineering

Georgia Institute of Technology, Atlanta, Georgia (1992)

Submitted to the Department of Aeronautics and Astronautics
in partial fulfillment of the requirements for the degree of

MASTER OF SCIENCE in AERONAUTICS AND ASTRONAUTICS

at the

Massachusetts Institute of Technology

February 1994

© 1994 Gregory W. Reich

All rights reserved.

The author hereby grants to MIT permission to reproduce and to
distribute publicly copies of this thesis document in whole or in part.

Signature of Author _____

Department of Aeronautics and Astronautics
January 21, 1994

Certified by _____

Professor Edward F. Crawley

MacVicar Faculty Fellow, Professor of Aeronautics and Astronautics

Thesis Supervisor

Accepted by _____

Professor Harold Y. Wachman

Chairman, Department Graduate Committee

Aero

Design and Modeling of an Active Aeroelastic Wing

Gregory W. Reich

Submitted to the Department of Aeronautics and Astronautics
in partial fulfillment of the requirements of the degree of

MASTER OF SCIENCE in AERONAUTICS AND ASTRONAUTICS

Abstract

The design modeling, and benchtop testing of a wing with strain and conventional flap actuation for vibration and flutter suppression is presented. The model hardware is described in terms of the design requirements. The design of an integrated safety system for flutter suppression is detailed. Model components are dynamically tested using an aluminum test article similar to the final design. Ground vibration testing and identification methods are developed using the testbench, and compared to finite element models to validate the analytical modeling. The actual model is tested using an electrodynamic shaker and accelerometers at a grid of points over the structure, and the model is identified using a frequency response-based method. The finite element model of the wing is validated via qualitative frequency response and node line contour comparisons with the identified model, and via quantitative measures of the modal frequencies and the Modal Acceptance Criterion. Finally, the validated analytical model is used for predictions of the aeroelastic behavior of the wing.

Thesis Supervisor: Dr. Edward F. Crawley
Title: MacVicar Faculty Fellow, Professor of Aeronautics and Astronautics

Acknowledgments

First off, I would like to thank my advisor, Ed Crawley, for his knowledge, help, and understanding in my helter-skelter, full-blast approach to getting a degree. There's got to be a better way to do it, but thanks for letting me do it my own way. I would like to thank Tienie van Schoor for his day-to-day help, support, and friendship. If I could give co-advisement billing to the thesis, the second, equally as important as the first, would be yours.

I would also like to acknowledge all of the members of the wing gang. It truly has been a team effort, you all deserve to be recognized. The wing gang is: Paul, Chris, Mark, Dina, Tienie, Charrissa, Kim, and UROPers Alfredo, Brian, J. P., John, and Enrique.

Grad school would not be the experience that it is without other students to share it with. To everyone in SERC, a big thank you for the times we have shared. Thanks go to Yool for putting up with me for the last year and a half (!). To Charrissa, thanks for the help and understanding, both technically and socially. You are a great friend and a wonderful person. I would also like to thank all of my other friends in the lab, especially Roger, Brett, Becky, Simon, Mark, Carl, Dina, and Kim, for providing me the excuse to do something besides work. Included in this boat are all of my friends outside the lab, especially Russ, and the rest of MIT grad soccer.

A big thanks must also go to my family. Unfailing support can sometimes be taken for granted, but this is the one time that I can publicly thank all of you for all that you have done. I cannot say enough about how much your support and love means to me. To Mr. and Mrs. L. W. Reich, and Mr. and Mrs. C. A. Shannon, my grandparents and the people to whom this thesis is dedicated, thank you especially for the long distance support.

This thesis is also dedicated to Christy, without whom I would not be the person I am today. Your thoughtfulness, dedication, and commitment to me have meant more than you know, or I can express properly. Wherever we may be, together or apart, you must know how much I appreciate you. I hope that I can have the chance to do the same for you someday.

Table of Contents

List of Figures

List of Tables

Introduction

Chapter 1

Aeroelastic wing vibration is a major concern to the modern aircraft engineer. Vibrations from gust loading or other sources affect the fatigue life and integrity of the aircraft structure. Gust loading also affects the ride comfort of the passenger. Instabilities such as flutter of wing or stores affects the maximum flight speed and endangers the integrity of the craft. Controlling gusts and other random vibrations helps reduce fatigue and ride comfort, while flutter suppression can increase the flight envelope and improve the safety of the structure.

Aeroelastic control of wing vibrations and instabilities is achieved by both passive and active means. Passive methods include structural tailoring of the wing, such as adjusting geometric sweep, or tailoring of the composite laminates used in the wing's construction. Active methods involve using the control surfaces of the wing as actuators. Recent studies have combined both of these methods.

A newer approach to aeroelastic control uses both active and passive methods, but is fundamentally different from other existing methods. Structural tailoring is used as it was before, shaping the bend/twist coupled

response of the wing that is desired. However, instead of control surfaces, strain actuators apply the controlling forces directly to the wing structure. In this way, many of the delays which hamper the conventional methods are circumvented: there are no hydraulics necessary to actuate the control surfaces, and there are no aerodynamic lags associated with the application of the control forces and moments.

Preliminary studies on aeroelastic tailoring investigated bend/twist coupling on cantilevered composite plates in a wind tunnel to verify analytically predicted flutter and divergence speeds [Hollowell and Dugundji, 1984]. Subsequent studies included geometric sweep in the models [Landsberger and Dugundji, 1985]. Active control techniques were being developed concurrently which were applied to flutter suppression experiments. Turner [1975] showed analytically that flutter suppression could be done on a high aspect ratio wing using an aileron as the actuator. In an international effort, wing-store flutter suppression was investigated on a 30% scale half span model of the YF-17 using leading and trailing edge control surfaces [Hwang, et al, 1980]. Free flight tests with a drone model were conducted to validate various control methods of flutter suppression [Newsom, Pototsky, and Abel, 1985]. Multiple leading and trailing edge surfaces were combined on a scale model of an "F-16 derivative planform" wing [Pendleton, Lee, and Wasserman, 1992]. Recently, aeroelastic tailoring was combined with control surface actuation in a series of tests on the Active Flexible Wing (AFW) program [Perry, et al, 1990]. The AFW model is a rigid fuselage, flexible wing scale model of an advanced tailless fighter. The wings are constructed of bend/twist coupled composite plates, and each wing includes two leading edge and two trailing edge control surfaces.

11

This conventional method of aeroelastic control has been used in the majority of flutter and vibration suppression experiments. This is primarily due to the existence of high-authority control surfaces on the wings in use. However, because these surfaces are not designed for this purpose, they are not necessarily the optimal actuators to use. The complete actuation mechanism includes significant aerodynamic and hydraulic lags because these actuators are typically hydraulic, and must generate aerodynamic forces to control the wing. In addition, ailerons typically operate over a limited bandwidth, which does not necessarily include the aeroelastic modes of interest.

Strain actuation is the alternative to flap actuation. Early studies in the use of strain actuation focused on characterizing the behavior of a certain type of strain actuators: piezoelectric, or piezoceramic, actuators [Crawley and Lazarus, 1991]. Analytical studies on the static aeroelastic behavior of wing models have been conducted [Ehlers and Weisshaar, 1990]. A simple two degree of freedom wind tunnel model demonstrated strain actuated flutter suppression [Heeg, 1992]. A more sophisticated experiment, demonstrating vibration and flutter suppression using multivariable control on a plate-like lifting surface with piezoelectric actuators, was successfully completed [Lazarus and Crawley, 1992]. This latter work forms the basis for the current study, which takes the technology developed by Lazarus and Crawley, and applies it to a larger, more wing-like model. The design and development for this program is presented by Lin and Crawley [1993].

The objective, then, of this research study is to investigate the effectiveness of a strain-actuated aeroelastic control system, and to compare its performance in gust alleviation and flutter suppression against a control-surface actuated control system on a wing flutter model. In this document,

12

the design and manufacture of the wing model, and issues in the development of the mathematical and experimental models required for verification, analysis and prediction of the structural behavior of the wing model are studied.

The finite element model is initially developed as an analysis tool to make intermediate decisions during the design process. Then, the design is constructed and experimental tests are run to identify the model. The finite element model is compared to the identified model to validate the analysis, and the analysis is iterated until the model errors fall within an acceptable bound.

The first section of this study explains the model hardware. Chapter 2 contains a description of the active wing flutter model in terms of the design requirements previously determined [Lin and Crawley, 1993]. All components are discussed in detail, and emphasis is placed on the method of attachment of one component to another. The description continues in chapter 3, where the design of an integrated safety system for flutter suppression is presented.

The second section of the thesis investigates the development and implementation of analytical and experimental modeling techniques for the program. The first part of chapter 4 describes the creation of a testbench model to replicate the "flight" hardware. The testbench will also used to develop experimental procedures for the identification of the wing model. These experimental models will then be compared to mathematical models as a validation of the finite element analyses. The second part of chapter 4 contains the application of these modeling techniques, both experimental and theoretical, to the wing model. The two models will be compared, and analysis on the similarities and differences presented.

Active Flutter Model Description

Chapter 2

2.0 Introduction

In order that the analysis and discussion that follows can be taken in context, it is desirable to first describe the physical set-up and hardware. An overall view of the active flutter model is pictured in Figure 2.1, which shows all of the major assemblies. The components of the active wing are built up on and around the spar, and include the piezoceramic actuators, the root attachment, mounting bracket and motor mount, the flap drive, the flutter stopper, and the aerodynamic shell. The design requirements for the project are covered in detail by Lin and Crawley [1993], and thus only the major requirements that affect each component will be discussed. This chapter contains a detailed description of each sub-component of the experimental hardware.

2.1 Wing Spar and Root Attachment

The spar is the load-bearing structure of the wing, and the foundation for the rest of the model. Its shape was required to be
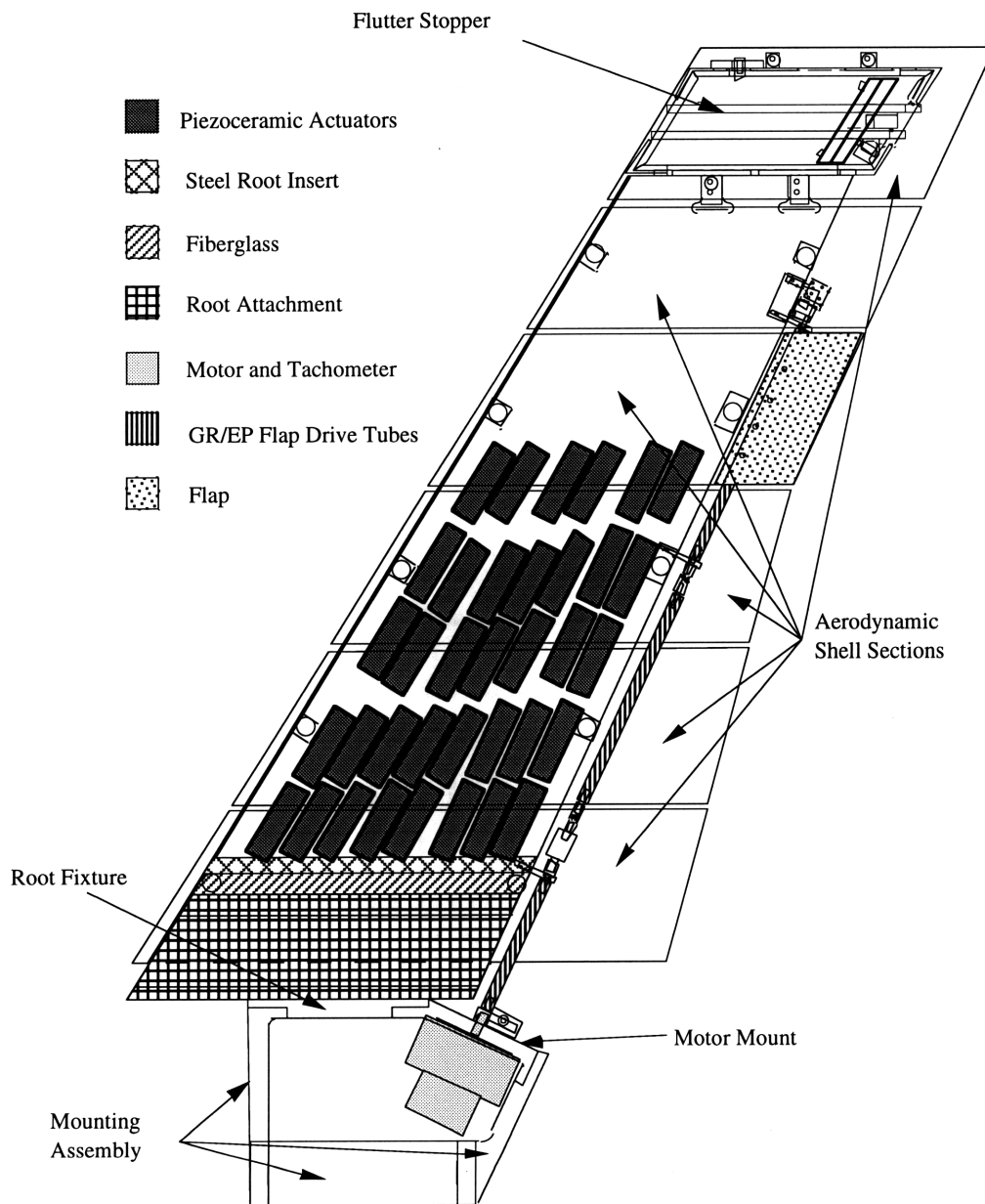
Figure 2.1: Top view of the active wing wind tunnel model

geometrically representative of aircraft wings in which bending/torsion flutter is critical, in order to compare its performance with real aircraft. Other design requirements included: the spar must have a flutter mechanism consisting of a coalescence of the first two modes; it must flutter well below transonic conditions; it must have modest structural

Figure 2.2: Spar dimensions and layout

thickness without necessitating the complications of a monocoque wing structure; and it must enable independent control of the first two modes by strain actuation.

To meet these requirements, a spar was designed and built from 2 IM7G/3501-6 graphite-epoxy plates of $[20°_2/0°]_s$ laminate. Each plate, 0.032" thick, is bonded to an aluminum honeycomb core 0.177" thick. The lay-up angles are referenced to the wing quarter-chord, which is swept 30° (see figure 2.2). This unsymmetric lay-up, combined with wing sweep, produces washout at the tip, as well as bend/twist coupling, which is instrumental in control of the torsional mode of vibration [Crawley and Lazarus, 1991]. The honeycomb core provides 2% structural thickness and allows enhanced bend/twist coupling.

16

Figure 2.3: Details of spar cross-sections

Figure 2.2 shows the physical dimensions of the spar (see Appendix A for physical properties of the materials). At the root, the honeycomb core is replaced with a 5.6" wide mild steel insert, and 4.75" wide fiberglass strips are added on top of the graphite-epoxy. The fiberglass strips consist of 3 layers of E-glass fabric, [0/90] lay-up, which increases the spar thickness by a total of 0.040". Cross sections A-A and B-B of Figure 2.2 are shown in more detail in Figure 2.3. Here the relative thicknesses of each material can be seen. The steel insert is designed to help relieve the high stress concentrations that exist at the root, and the fiberglass layers are designed to protect the graphite-epoxy and insure a smooth joint between the spar root and root attachment. The hole pattern for the root attachment bolts is also visible in Figure 2.2, as well as the eleven solid aluminum inserts replacing the honeycomb around the periphery of the spar. These allow for other attachments to the spar, such as the flap drive bearing mounts (Fig. 2.6), the shell (Fig. 2.7), and the flutter stopper (Fig. 3.2). The two inserts for flutter stopper mounts on the wingtip have tabs to prevent shear pull-out from the spar due to centrifugal forces.
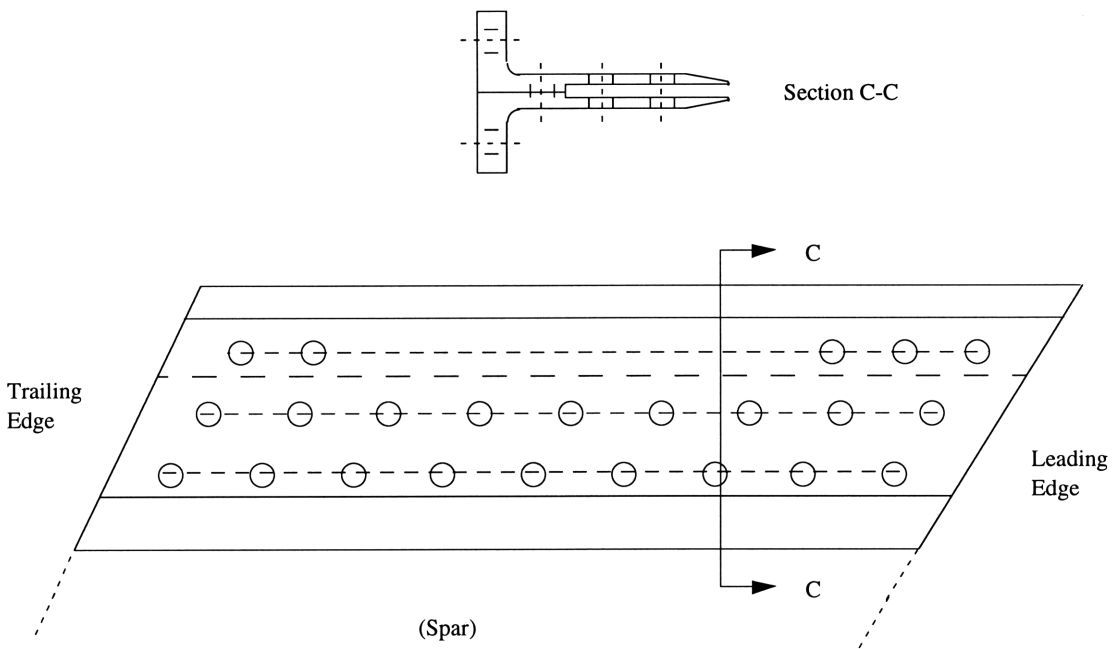
Figure 2.4: Cross-section and top view of root attachment, including bolt pattern

Figure 2.4 shows two views of the root attachment. The spar slides into the slot, and is secured by eighteen 1/2" diameter steel through bolts. The root attachment enforces a near cantilever boundary condition by transferring loads to the root fixture, and from there to the rigid wind tunnel support, as shown in Figure 2.5. The mounting assembly, all
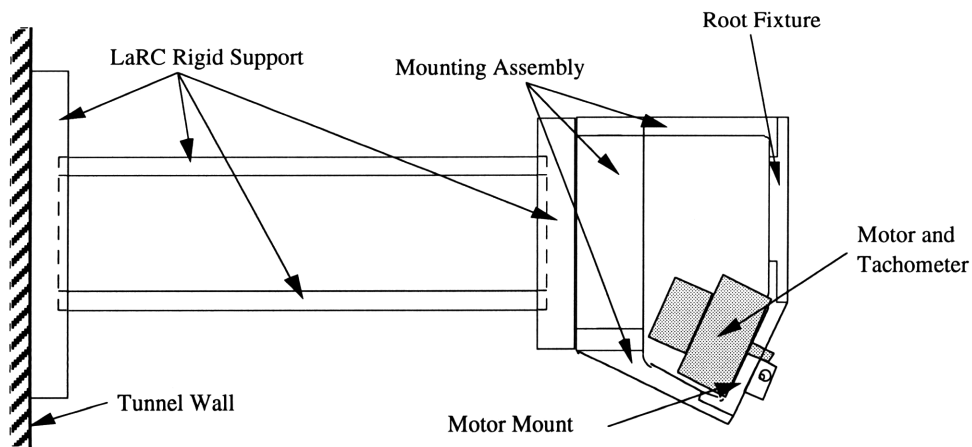
Figure 2.5: Wind tunnel support structure and mounting assembly interface

machined aluminum plates, serves as an interface between the spar and the LaRC rigid support, which extends several feet out from the wind tunnel wall. To isolate the model aerodynamically from the mounting structure, a splitter plate (not shown) was used. This 4' x 8' aluminum panel was mounted vertically at the root fixture to separate the wing assembly from the mounting assembly.

2.2 Piezoceramic Actuators

Strain actuation is carried out by the 72 piezoceramic actuator packages mounted on the top and bottom of the spar, pictured from above in Figure 2.6. The actuators covered 63% of the region between the 13% and 66% span locations. This coverage is approximately between the root attachment and the flap. Figure 2.7 shows a single package, which consists of 4 G-1195 piezoceramic wafers, two wide and two thick. The packages were made by imbedding the wafer stacks in kapton tape, and covering with a layer of polyurethane.

The amount (thickness) of wafers to be used was determined in a series of trade studies done by Lin and Crawley [1993] which indicated that
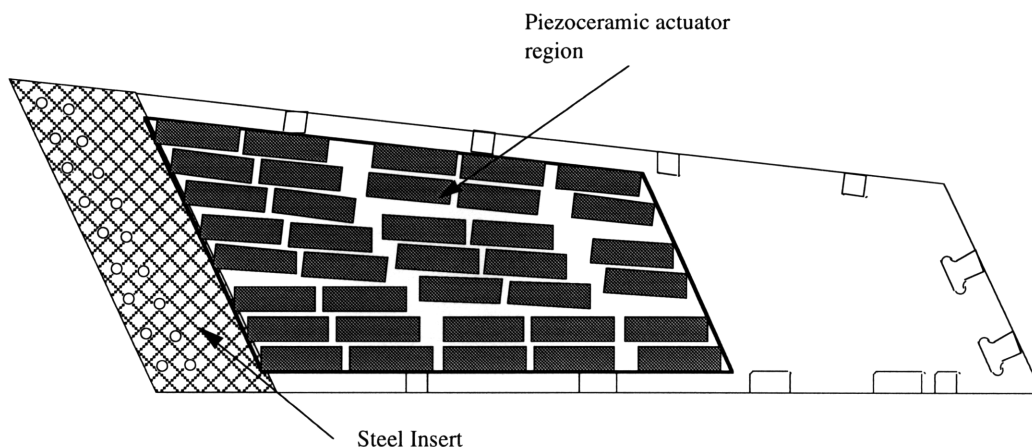
Figure 2.6: Piezoceramic package placement on wing
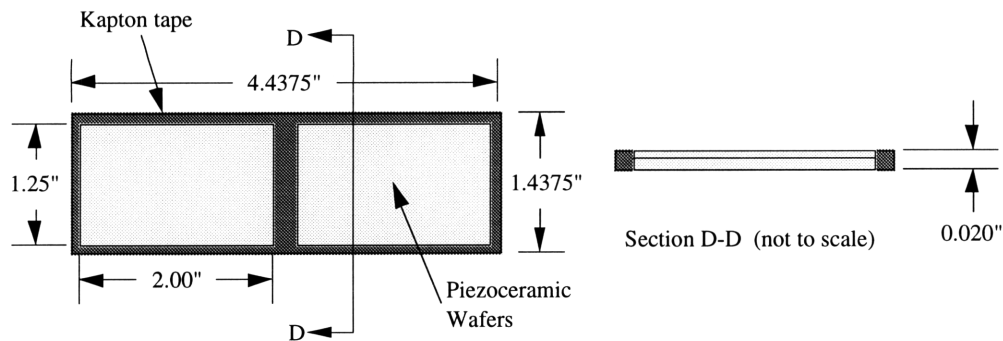
Figure 2.7: Top view and cross-section detail of one piezoceramic actuator package

while there is increasing authority on the bending mode as actuator thickness increases, there is an optimum thickness for torsional control. Because simple piezoceramics are elastically and piezoelectrically isotropic, they cannot provide shear strain, and thus do not have any authority over torsional motion. With an orthotropic plate, such as the spar, torsional control is possible because of the bend/twist coupling produced by the non-symmetric lay-up of the graphite-epoxy [Lazarus and Crawley, 1989]. As the actuator thickness is increased, however, the effects of the elastically isotropic actuation material begin to dominate the effects of the orthotropic plate, reducing the bend/twist coupling. The optimum thickness in this case was found to be 0.020".

Strain actuation is applied by poling packages on opposite sides of the spar in opposite directions. The resulting strain is realized as a bending moment on the spar. The modal forcing is then controlled by arranging the actuator packages into fifteen blocks. These blocks are then arranged into actuation groups for control of two modes: one bending and one torsion. For bending, all of the blocks are actuated in the same direction. For torsion, the blocks are divided into two regions, roughly span-wise, and are actuated in opposing directions from each other. The grouping is ordered such that
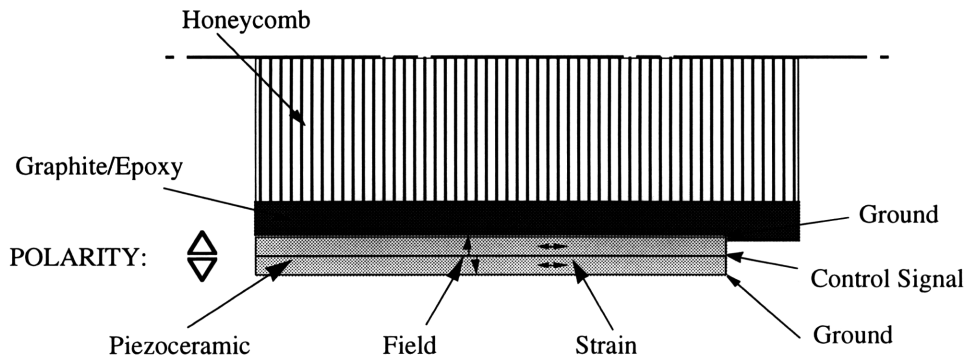
Figure 2.8: Detail of spar cross-section with piezos and applied signal (not to scale)

the two opposing regions of strain actuation are on opposite sides of the zero-curvature line for the torsion mode. Figure 2.8 shows the lower half of the spar cross-section with packages, and how the control signal is applied between layers of wafer, so that both the spar and the exposed surface are grounded. Each block of packages, consisting of four to six packages, is powered by one power amplifier, with a maximum of ±200 volts, which is roughly 2/3 of the coercive field strength of the piezoelectric material.

2.3 Flap Drive System

The flap drive system design was driven by the large size of the electric torque motor necessary to drive the flap. The impossibility of mounting the motor just inboard of the flap dictated that the motor be placed outside of the wing in the mounting assembly, and connected to the flap by a long drive shaft. The shaft would have to be sectioned and joined with universal joints or other flexible members, due to the significant bending of the spar under operational loads, to allow for clearance within the aerodynamic shell. The drive shaft was also required to be extremely stiff in torsion to minimize the windup, and consequently maintain a high

level of flap motor authority over the actuation range. A sensor for measuring the flap angle would also have to be included in the design, and a local flap servo built to allow control of the flap angle from commanded inputs.

The drive system that developed is shown in Fig 2.9. The design centers around 3 hollow AS4/3501-6 graphite-epoxy shafts, each with a [±45°] lay-up repeated for maximum torsional strength. Zero-backlash steel universal joints from Sterling Instruments are used between shafts to allow the flap to operate when the wing underwent large deflections. A GTC telescoping ball spline allows for axial play, and the drive is attached to the spar at three locations with mounts which hold miniature ball bearings. The whole drive system has ±0.15° windup at nominal operational torque levels due to aerodynamic loading on the flap.

The PMI U12M4HA pancake style torque motor and PMI U6T
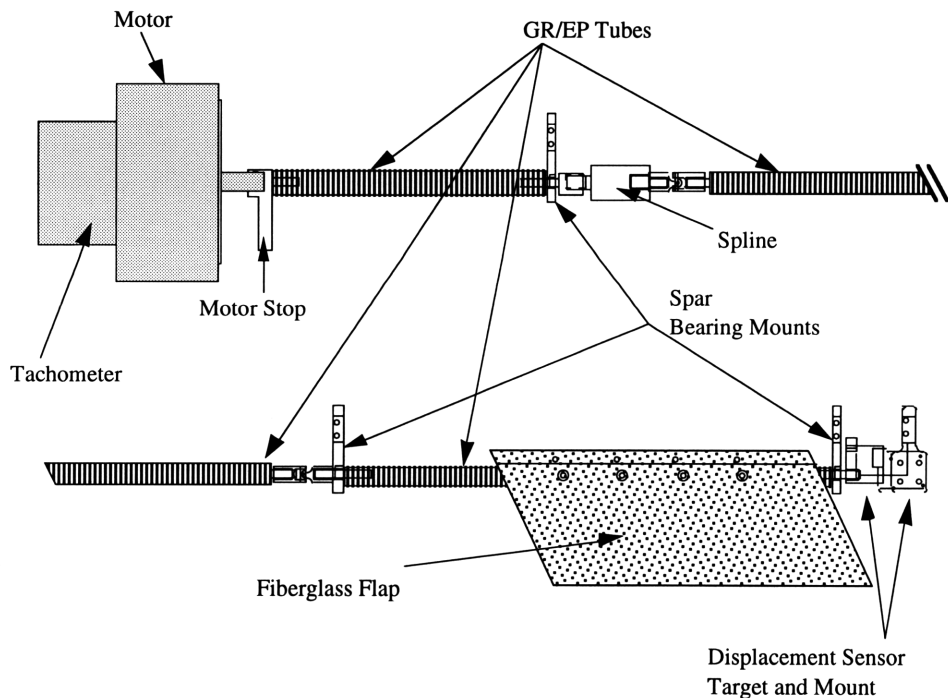
Figure 2.9: Flap drive system

tachometer are mounted to the motor mount, which is angled to match the trailing edge sweep angle (see Figure 2.5). The motor mount is part of the mounting bracket assembly. Hard stops are added to limit the rotation of the motor to ±6°. This protects the flap drive from over-rotation and the starting transient which the motor undergoes.

This system drives a flap that is 20% in both span and chord, and is located between the 60% and 80% span locations. The only requirement on the flap drive system was that the flap have enough chordwise stiffness to assume chordwise rigidity in the model. The flap is made from MXB-7251/181 fiberglass fabric of $[0/45]_s$ laminate, with a wall thickness of 0.040", and is mass balanced to decrease the complexity of the controller. The flap is bolted directly to the shaft (see Figure 2.10). Flap position is measured with a Kaman KD-2310-2UB inductive non-contact displacement sensor which targets an eccentric cam, whose relative location is pictured in Figure 2.9. The cam's slanted face moves perpendicularly with respect to the sensor when the shaft rotates. The ±5° of flap angle is translated into a 0.080" travel of the cam face. Hard stops on the cam prevent it from over-rotating and destroying the sensor.
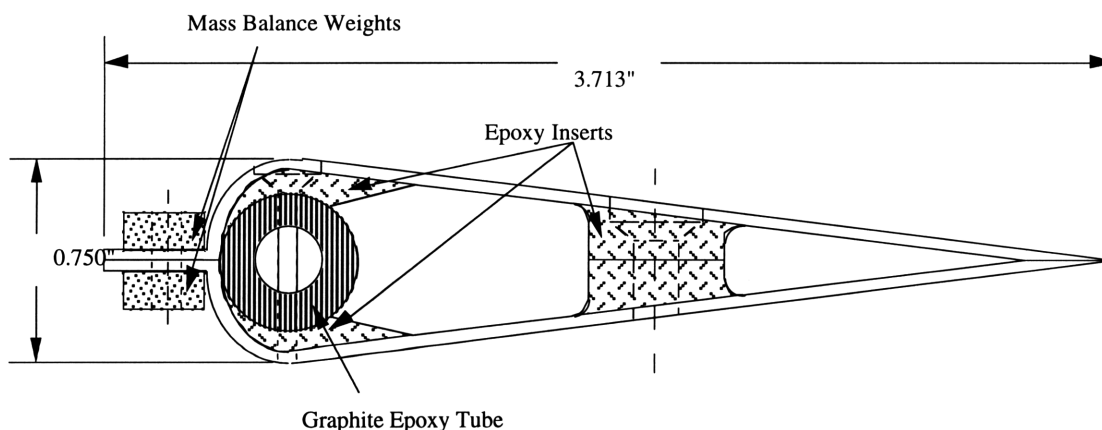
Figure 2.10: Cross-section of the flap

23

2.4 Aerodynamic Shell

In order for the model to be tested with a proper aerodynamic loading, a light-weight fiberglass shell was designed to cover the model and "shape" the aerodynamics. The requirements for the shell were defined as: the wing geometry should be representative of aircraft in which bending/torsion flutter is critical; the airfoil shape should not provide any lift at zero angle of attack; and the shell should not add appreciable stiffness to the spar. Adding stiffness would alter the structural dynamics and diminish the control authority of the actuators.

A sectioned fiberglass shell, made of MXB-7251/181 fabric in a $[0/45/0]_s$ laminate, was designed to provide these qualities. The 0.060" thick shell is shaped like a NACA 66-012 airfoil, divided into 5 spanwise sections, and fixed to the spar in only two locations per section (see Fig. 2.11). The shell completely envelops the spar and attached components. Its removable section design allows easy access to internal hardware. Each shell was designed as two half shells, bolted together through the spar at the leading
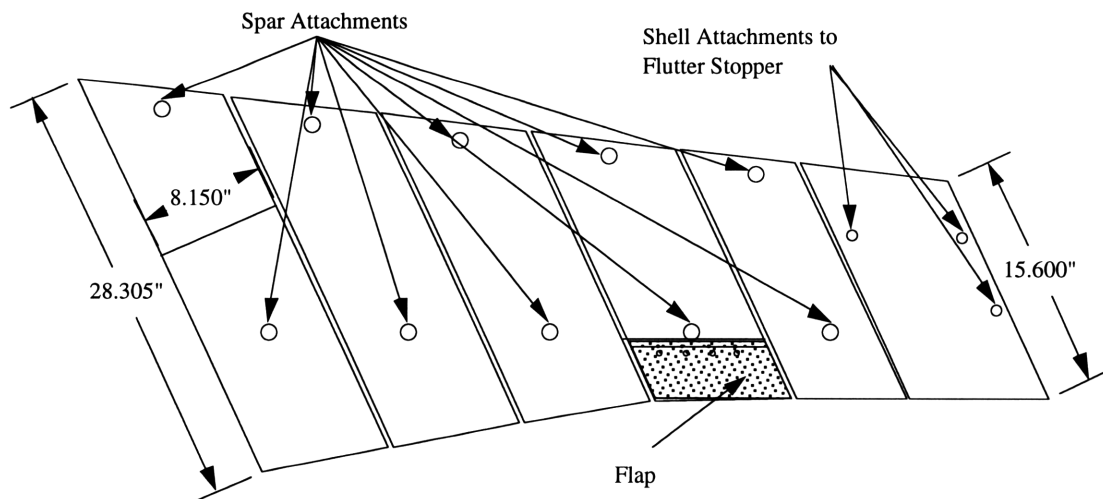
Figure 2.11: Location of shell attachments to spar and flutter stopper

and trailing edges. Figure 2.12 shows a detail of an attachment point on a typical shell section. The shell over the wingtip, which covers the flutter stopper, is attached in a slightly different manner.

The inserts are made from an epoxy that was bonded to the inner surface of the fiberglass after curing. This epoxy is hard enough to hold a tap, so inserts threaded on both inner and outer surfaces are bonded to the epoxy. These hold the bolts which pass through the spar and attach the two sides of the section. At the leading edge, the top half is made with a lip that overlaps the bottom half, so that the halves cannot separate during testing, allowing airflow through the shell. A filler is used at the leading and trailing edges, at the front for greater strength, and at the back for a good mating surface between top and bottom halves. Because a 0.30" chordwise gap remains between shell sections for clearance when the spar bends, foam is inserted between sections so that no air can flow under the shell.
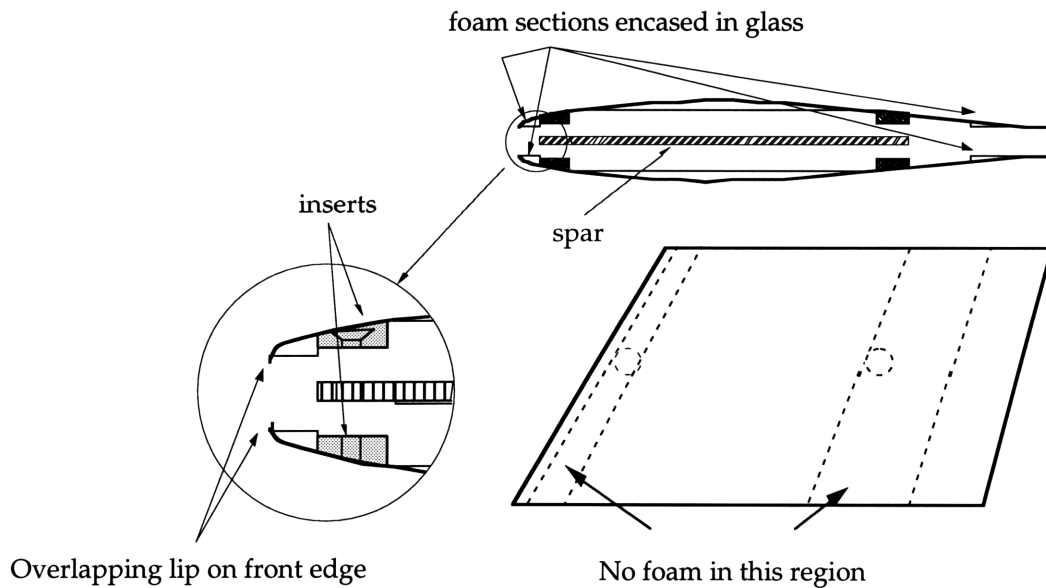
Figure 2.12: Detail of a "typical" shell section

2.5 Flutter Stopper

In order to test the flexible flutter model in the wind tunnel, provisions for both the model's and the tunnel's safety are taken. Tunnel shut down is not an acceptable approach because the response time of the tunnel is much slower than necessary. Some other mechanism is required that can respond in the time interval of one or two vibration cycles. A mechanism that quickly changes the wing's aeroelastic properties at any given flight speed was designed and built. The system includes several sensors to detect the onset of flutter, which then trigger the firing mechanism. The system is the subject of the next chapter, which describes in detail the design and testing of an integrated flutter suppression system.

Integrated Flutter Suppression System

Chapter 3

3.0 Introduction

As discussed briefly at the end of the last chapter, the wing design includes a safety system which aeroelastically stabilizes the model after the onset of flutter. The change in aeroelastic properties of the wing is accomplished by shifting the wing chordwise CG location, which causes a significant change in the stability of the wing at a given tunnel velocity. The CG shift is achieved by sliding a large mass forward along the tip of the wing. The flutter speed of the wing with the mass in the "undeployed" position is considered the nominal flutter speed of the system. Approximately 30% above this speed is the "deployed" flutter speed, where the mass is located in the forward, or deployed, position. This is the highest speed at which the wing can be safely tested, since the wing is aeroelastically unstable for either configuration at speeds above this point. This chapter discusses the design of the internal, integrated tip mass flutter stopper, both in terms of its functional requirements and the resulting design.

Flutter stopper systems are not an innovation in aeroelastic wind tunnel projects. As evidenced by the wide variation in types of flutter suppression devices, there are many different mechanisms of preventing or suppressing instabilities, and therefore the potential destruction of the model. Some simple designs physically restrained the model using stops or other dampers [Ricketts and Doggett, 1980]. More complicated systems encompassed the use of a wingtip or underwing store, designed to decouple the dynamics during flutter from the rest of the wing [Noll, et al, 1989]. Ejectable ballast have also been used to change the aeroelastic properties, although this is not optimal for the wind tunnel setting [Newsom, Pototzky, Abel, 1985]. The current design is based on a system used on the YF-17 flutter model program [Hwang, et al, 1980], which housed a sliding mass inside an AIM-7S wingtip store. However, as will be emphasized below, a store could not be used for this experiment, and the sliding mass was made internal to the wing cross-section.

3.0.1 Design Goals and Functional Requirements

The set of specifications that any design must meet is referred to as the functional requirements [Suh, 1990], which can represent performance goals, constraints, regulatory, or safety requirements. There are five functional requirements listed in Table 3.1 which were to be met in order to achieve the design objective. Several of these were not absolute requirements, and were not posed as such. Rather, they were guidelines to steer the design during its development.

Table 3.1: Functional requirements and design goals for the flutter stopper

Designation	Requirement
R1	Increase the open-loop flutter speed by 30% in velocity
R2	Fit within the volume available inside the aerodynamic shell
R3	Deploy within two complete cycles at the expected flutter frequency, with a +5° slope, and keep positive pressure on the mass in the deployed position
R4	Incorporate multiple levels of redundancy in the trigger in case of one or more failures
R5	Minimize the weight and span of the support structure

3.1 Flutter Stopper Hardware

As a first step in the design, it was necessary to determine how much mass was needed to meet requirement one of Table 3.1. This was accomplished in a trade study done by Lin and Crawley [1993]. They investigated some of the design parameters (physical properties) which could be varied, including size, weight, and CG location, and the effects that these had on the flutter speed of the wing in the deployed versus undeployed configuration. The analysis was done using a five mode Rayleigh-Ritz structural model of a multi-layered composite plate using unsteady, swept two-d strip theory aerodynamics with a one pole approximation of Theodorsen's function. This code was adapted from an earlier work by Lazarus and Crawley [1992]. The results of the study showed that a 1.5 kg

(3.3 lb.) mass, shifted from "slightly aft of the midchord" to the leading edge at the wingtip, would result in an increase of 30% in flutter speed.

Once the amount of mass needed was determined, completion of the design required refinement and compromise necessary to meet the remaining requirements. For example, in reality it was not possible to put the mass CG at the leading edge, since this would have caused the assembly to extend in front of the leading edge. This would have violated the second requirement (R2), which was to fit the entire structure inside the shell. The effects of this requirement are felt throughout the design.

Due to the rigorous volume constraints imposed by R2 and R5, a tungsten alloy was chosen as the material for the translating mass. This alloy (pure tungsten is more dense, but nickel and copper are added to improve machinability) is 50% heavier than lead, at approximately 0.6 lb/in.^{3}. Many design iterations were performed varying the cross-sectional shape, width, and CG locations of the mass in an attempt to minimize the size and still meet all of the requirements.

The schematic problem of deployment is pictured in Figure 3.1. The initial and final locations x_i and x_f were chosen to be aft of the mid-chord, and as close as possible to the leading edge.. The spring size and strength were
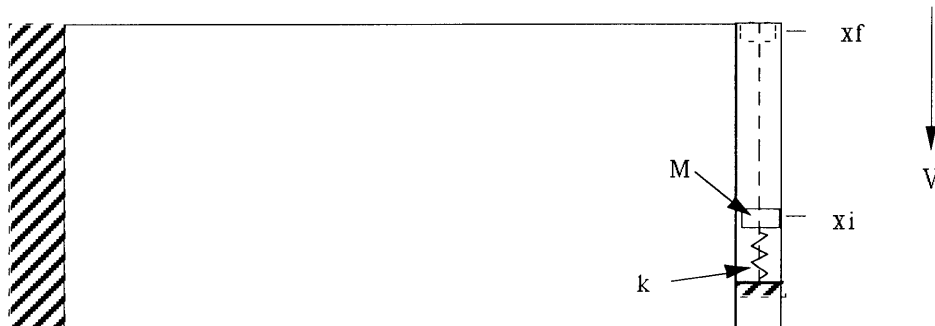
Figure 3.1: Mass deployment schematic

chosen by solving the dynamic spring-mass problem to satisfy the deployment requirement (R3). Because of the predicted torsional motion of the wingtip during flutter, the deployment was chosen to be up a constant 5° slope (angle of attack). This did not reflect the physical motion that the system would undergo, but simply increased the strength of the springs to meet the requirement. For a given deployment time, in this case two cycles at 8 Hz, or 0.25 seconds, the spring constant and spring length were inter-related. The longer the spring, the softer it could be. Of course the spring must also satisfy the geometrical constraints imposed by the spring's fully compressed solid length and inner and outer diameters. The springs were also chosen to meet the requirement that their compression length be longer than the travel distance, so that even in the deployed configuration the springs would be imparting a forward force on the mass. In order to provide redundancy in forward retention once deployed, a spring latch was added just behind the deployed mass location. Rubber bumpers were affixed to the front of the mass to cushion the collision with the leading edge frame.

Figure 3.2 shows both top and cross-section views of the completed flutter stopper. The entire assembly fits inside the NACA 66-012 airfoil shape with chord equal to 15.6 inches, which is the chord at the tip of the shell. Both frame and mass are swept 31.9°, which is the sweep of the leading edge of the shell. The mass is tapered on its forward and rearward facing sides to maximize the distance between fore and aft positions. Both inboard and outboard frames are similarly tapered, since these must extend further than the tungsten in both directions. The frame is made from 1/4" to 1/2" thick aluminum beams, designed for maximum stiffness with minimum weight (R5). For this reason they are channeled wherever possible, and connected at each corner with steel brackets.

31
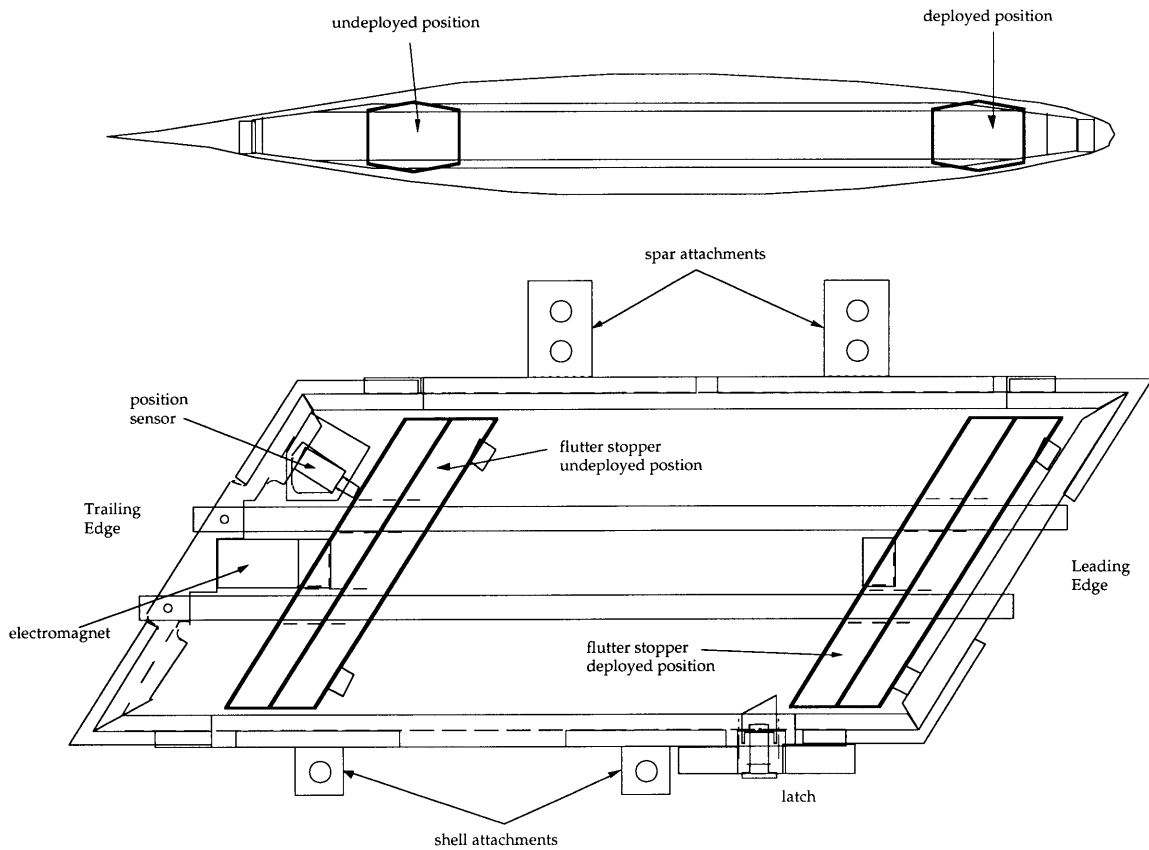
Figure 3.2: Cross-section and top view (assembly drawing) of the flutter stopper

The mass slides on two 3/8" diameter hardened steel rods. Two runners are used, as opposed to a single runner, to cut down on the possibility of rattle occurring. The rods are pinned into the trailing edge frame, and are held in alignment at the leading edge by precision-machined through holes. Their size and strength were chosen so that the bending frequency of the rods with the mass in the middle, the worst case scenario, was greater than 30 Hz.

The flutter stopper is attached to the spar with brackets at the two inserts on the wingtip, located at approximately the 30% and 60% chord locations. These aluminum brackets slide over the spar, and are bolted through the aluminum inserts. The aerodynamic shell is attached at three locations: two aluminum outboard blocks, and at the 30% chord spar

attachment. The outboard blocks were designed to mimic the spar where the shell bolts through it, and the shell is fastened in the same manner as at further inboard locations over the spar. It was determined that this three-point attachment method is acceptable, since there was predicted to be little deflection, if any, of the flutter stopper relative to the wingtip.

The safety electronics of the flutter stopper were designed to monitor sensors for signs of impending flutter, deploy the tungsten mass, and shut down all critical activities during deployment. In the undeployed configuration an electromagnet holds the mass via an iron target on the trailing edge of the tungsten. The mass is deployed when the safety circuit shuts off power to the magnet. The circuit monitors different sensors on the wing, and responds to input from several locations. If any one of the indicators is tripped, then the mass is deployed, the tunnel shut down, and the control signal to the strain actuators cut off. The multiple sensors used to meet R4 are: (1), a single spike threshold limit on one of several strain gages at the root, just outboard of the root attachment; (2), operator input from the control room; (3), accidental deployment by the magnet/target interface, which is monitored by a push-button switch at the undeployed position; and (4), power failure, in which case the mass is released and everything shut down.

The flutter stopper was mounted on the testbench described in the next chapter and tested for accidental and deliberate deployment at ±3.25" tip deflection at 3 Hz and at ±5° twist at 16 Hz. Accidental deployment is defined as deployment due to premature release by the magnet. Deliberate deployment means that when deployment is initiated, the mass covers the entire span and latches at the deployed position without binding in transit. A series of tests were done at both resonances to verify that the mass never

deployed at the tested vibration levels, but, once deployed purposely, the mass deployed cleanly and latched properly.

Table 3.2 summarizes the physical dimensions and predicted performance parameters of the design. Appendix A contains more detailed information on the material properties of each flutter stopper component. The predicted aeroelastic performance listed here is from the preliminary analysis of Lin and Crawley[1993].

In Chapters 2 and 3, the description of the design for the wind tunnel project has been presented. The development of testing, modeling, and analysis procedures for the wing is outlined in the first part of Chapter 4. These procedures were then used to analyze the composite wing, and results of this can be found in the latter section of Chapter 4.

Table 3.2: Dimensions and properties of the flutter stopper

Properties of the translating mass:	
Density	0.615 lb./in.^{3} (1.7 x 10^{-5} kg/mm^3)
Length (chordwise direction)	1.400 in. (35.56 mm)
Width (spanwise direction)	4.480 in. (113.79 mm)
Maximum height	1.100 in. (27.94 mm)
Weight (includes target and stops)	3.364 lbs. (15.000 N)
Frame Properties:	
Length	13.227 in. (335.97 mm)
Width	5.728 in. (145.49 mm)
Maximum height	1.000 in. (25.40 mm)
Weight (everything but tungsten)	3.053 lbs. (13.614 N)
Spring Properties:	
Stiffness (each)	0.265 lb/in. (0.047 N/mm)
Free Length	11.500 in. (292.1 mm)
Length - Deployed Position	10.455 in. (265.56 mm)
Length - Undeployed Position	1.700 in. (43.18 mm)
Mass CG travel	8.755 in. (222.38 mm)
Mass CG Undeployed chord location	68.62 %
Mass CG Deployed chord location	12.49 %
Magnet strength	12.0 lbs. (53.5 N)
Deployment time	0.225 sec.
Undeployed flutter speed (predicted)	155.8 ft/sec (47.5 m/sec)
Undeployed flutter q (sea level)	28.88 psf (1383.1 N/mm^2)
Deployed flutter speed (predicted)	199.8 ft/sec (60.9 m/sec)
Deployed flutter q (sea level)	47.47 psf (2273.5 N/mm^2)
Flutter speed increase	1.282 %
Flutter q increase	1.644 %

Model Testing, Identification, and Results

Chapter 4

4.0 Introduction

Before a finalizing a design, engineers often build a full-sized model, or testbench, as a verification of the geometric interactions between components. If the dynamics of the model are similar to that of the real hardware, then components can also be tested at dynamic conditions similar to operating conditions. In addition, experimental and analytical techniques to be used on the final design can be developed using the testbench. The first section of the chapter contains a description of the testbench program. A method of structural dynamic experimental model identification is developed using the testbench, and, in parallel, a finite element model of the testbench is constructed. The two models, experimental and analytical, are compared in section 4.3. The entire process: experimental identification, finite element modeling, and model comparison, is repeated for the composite spar, and this is covered in sections 4.5-4.6.

4.1 Testbench Description

A 0.25" thick aluminum plate, possessing the same planform as the composite spar, is built as a testbench to gain insight into likely problems that might be encountered with the flight hardware. Its purpose is to be a platform from which the flap drive system and flutter stopper can be tested for fit and for dynamic performance. As a flexible model, the testbench is required to meet the following requirements: the flap drive system and flutter stopper should be attached to the testbench in the same manner and at the same locations as attached to the spar; the testbench should allow static deflections of at least 2", to match the predicted (steady) operational aerodynamic load deflection; the first bending frequency should approximately 3 Hz to match the predicted fundamental frequency of the composite spar; and, oscillations at this frequency should be approximately ±6.3", based on an estimated flutter amplitude of 15% of the span.

The testbench that is built meets or almost meets every specification. The fundamental bending frequency of the testbench is approximately 3 Hz, and oscillations of ±3.25 inches are attained at the tip at this frequency. The target vibration amplitude is not met because of the stroke limit and placement of the shaker, not a limitation on the testbench itself. In addition, the second mode frequency is measured at approximately 16 Hz, and ±5° of twist are recorded at the outer frame of the flutter stopper. With the flutter stopper attached, the testbench has a static deflection of 0.6875" inches by gravity loading alone. A static deflection of 2" inches is recorded with a 15 lb distributed load.

Once the testbench is built, and components mounted, a system for component testing and model identification can be assembled. The test set-up is pictured in Figure 4.1, which shows a side view from floor level. The
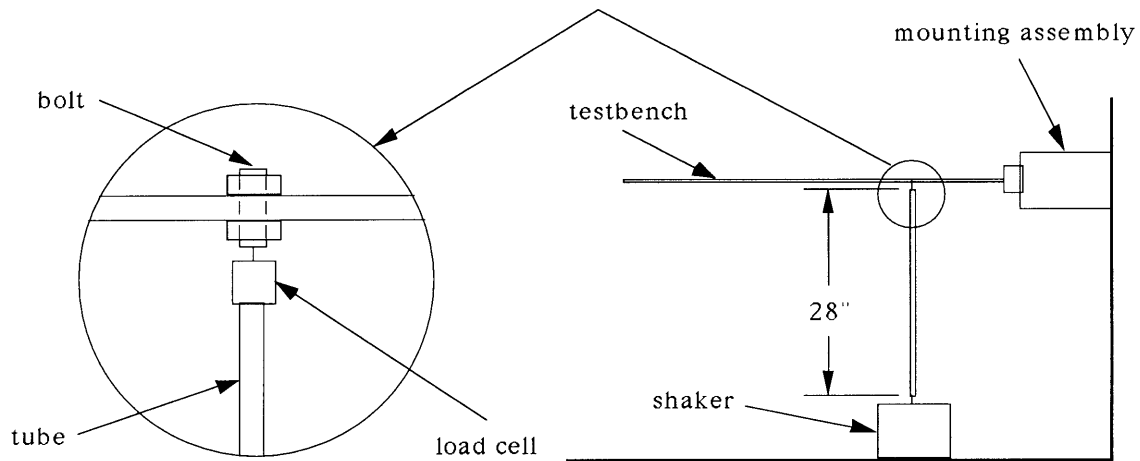
Figure 4.1: Experimental test setup

testbench is mounted to the wall *in-situ* via the "real" root attachment and mounting assembly, which allows a check on these components to determine whether or not they provide a rigid base on which to mount the wing. A Ling 420-1B electrodynamic shaker, the disturbance source, is located on the floor underneath the testbench, and is connected to the plate via a 28" long hollow tube stinger. The stinger has 0.125" long sections of piano wire at each end, which act as moment releases and prevent any eccentric forces from reaching either the motor or the testbench. The stinger is attached to the testbench through a force transducer, and then a 0.25" diameter bolt which passes through a hole drilled in the plate. The bolt is then fastened to the testbench from above and below with hex nuts.

This set-up is unconventional for several reasons. The first is that while typical ground vibration tests (GVTs) also utilize shakers with stingers, these shakers are normally hung above the model with springs which uncouple the dynamics of the shaker from those of the structure. The shaker is placed on the floor beneath the structure for two reasons: convenience and ease of movement. The justification for placing the shaker on the floor is that

for a single shaker, as long as the load is measured at the actuation point where it is applied to the structure, the dynamics of the test structure completely uncouple from the stinger, shaker, and shaker mount. The length and stiffness of the stinger is not an issue for this reason as well. The second reason that this setup is unconventional is that the structure has been changed to attach the disturbance source. However, a 0.25" diameter hole in an aluminum plate 17" wide has negligible global effect on the response of the system.

4.2 Structural Dynamic Model Identification

This section describes the development of an identification method to be applied to the testbench. Single input, single output (SISO) frequency response functions (FRFs) are measured at defined positions on the testbench. This data is input into a program which identifies the system model. The identified model can then be manipulated to extract frequencies, mode shape, and other modal information.

A Tektronix 2630 Fourier Analyzer is used to drive the shaker and record the output from sensors. The shaker is driven by a Crown DC-300A power amplifier, and acceleration is measured via an Endevco 7701-50 accelerometer and Endevco 2721 charge amplifier. Input force is measured using a PCB 208B load cell and PCB 484B charge amplifier. Frequency response functions of transfer functions (TFs) from the load cell input to acceleration output are measured at each of the selected points on the testbench in both the flutter stopper undeployed and deployed configurations for random noise inputs in the 1 to 100 Hz range. Data is averaged over 10 consecutive measurements.

The forty-four sensor locations are carefully selected to adequately represent the important lower modes of the system with a minimum number of states. Because more modal information exists near the tip of the wing, especially for higher modes where there may be several node lines closely spaced, more points are chosen at the tip (see Figure 4.2). Only the four corners of the flutter stopper are chosen as data points, because it is expected to act as a rigid body. Note that in the finite element model, it is not assumed to be a rigid body. Aside from these four points on the flutter stopper, all of the points chosen are on the plate itself.
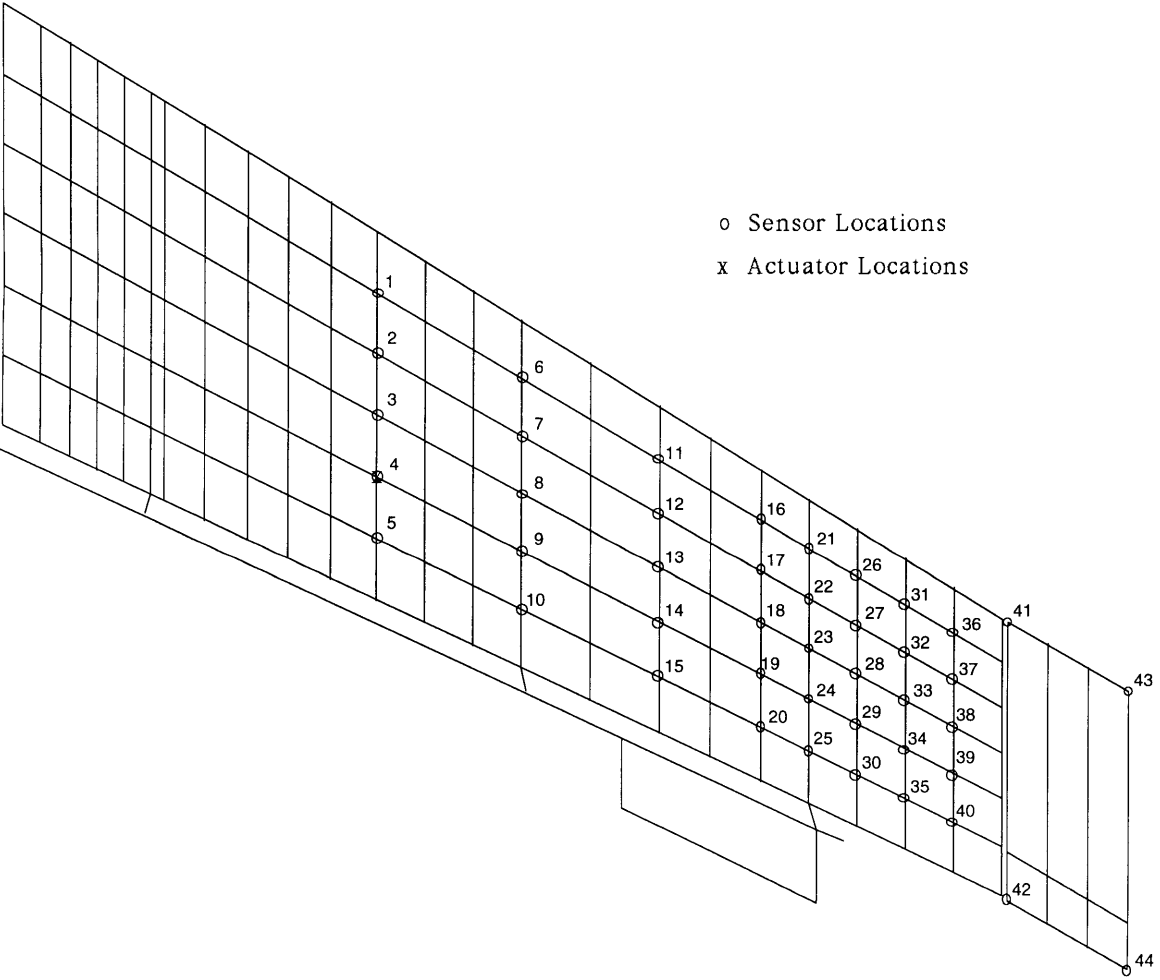
Figure 4.2: Sensor and actuator locations on the FEM grid

The forty-four locations are chosen such that they coincide with nodes from the finite element mesh. This greatly simplifies the process of comparing the experimental model with the finite element model. The actuator location, location 4, is chosen to be a gridpoint location as well, so that a direct comparison can be made with transfer functions from the finite element model. Figure 4.2 shows the actuator and sensor locations on the testbench finite element grid.

Some data manipulation is required prior to identification of the system. The experimental FRFs were measured in terms of accelerations, however, modal information for analysis and aeroelastic predictions are usually in the form of displacements. This requires that the data be converted to functions with outputs of displacements, which entails dividing the value of the transfer function at each frequency ω (in Hz) by $4\pi^2\omega^2$. The electronic gains from sensors and charge amplifiers are also included. In addition, the low-frequency ($<\sim 2$ Hz) information is ignored because the Endevco charge amplifier used in conjunction with the accelerometer has a low-frequency limit at about 2 Hz. All of the data below this point is suspect, and should not be included in the data. This could be prevented of course by using a charge amplifier with a lower low-frequency bound.

System identification is accomplished using a curve-fitting technique on the measured frequency response data [Jacques and Miller, 1993]. The technique logarithmically fits the FRFs by varying the frequency, residue, and damping ratio of each pole. The model is initialized with fewer states than required, and aggregated to match the number of states that physically exist in the system. This requires some prior knowledge of the system response, as any number of states can be used to fit the data. The result of the fitting procedure is a 1 input, 44 output SIMO (Single input, Multiple
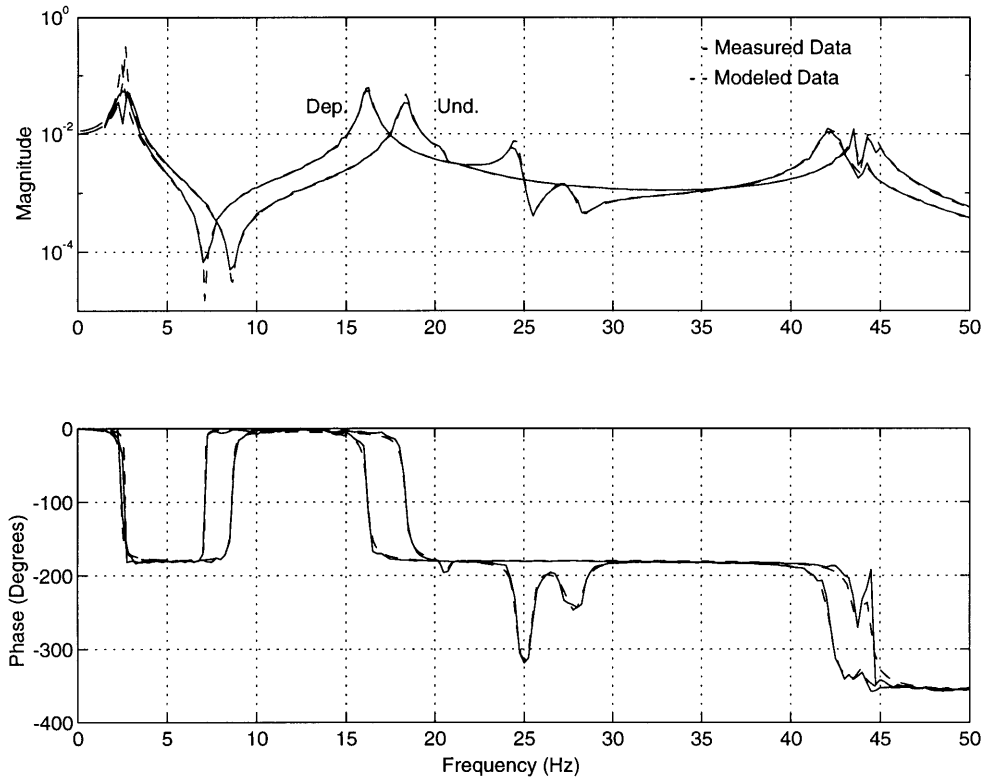
Figure 4.3: Frequency response functions for measured data and identified
system of the testbench at location 27

output) state-space system matrix describing the dynamics of the system at the output locations. Figure 4.3 shows the Bode plots of the frequency response from one SISO transfer function, load cell (location 4) to displacement at location 27. The raw data and the identified system are included for flutter stopper deployed and undeployed models.

The quality of the fit, and therefore the identified (modal) model, is dependent on several factors. The most important of these is the frequency resolution of the data in the discretized transfer function. If the data is taken with a wide frequency spacing, then the pole locations and damping ratios may not be accurately represented in the raw data. The result is that the

system identification procedure produces a model which does not as closely resemble the behavior of the actual test piece. The identification algorithm can only be as good as the quality of the data taken.

From the identified model, the natural frequencies and modeshapes are extracted for analysis and comparison with the finite element model. This comparison is found in the following section. The modeshapes of the experimental models for flutter stopper undeployed and deployed cases are plotted in Appendix 4A, along with the corresponding FEM modeshapes.

4.3 Finite Element Model of the Testbench

This section focuses on the development of an analytical model of the testbench using the finite element modeling program ADINA. The purpose of constructing a finite element model (FEM) of the testbench is to act as a validation of the analytical modeling process for the composite spar. The testbench model is in fact based directly on the finite element model of the composite spar, which had been used previously for design decisions. If the analytical model is shown to accurately predict the response of the testbench, then confidence is gained in the analytical model of the composite spar.

The finite element mesh of the testbench model is pictured in Figures 4.4 and 4.5. Figure 4.4 is a three-dimensional view of the wire-mesh grid, which highlights the vertical region of the root attachment. Figure 4.5 pictures the different element group regions of the model. The testbench and root attachment are divided into 6 chordwise elements and 24 spanwise elements. The root attachment is modeled as a vertical plate attached to a horizontal plate, which is represented in regions 1 and 2 of Figure 4.5. The horizontal plate is split into a three-layered plate where the testbench fits into the root attachment slot, regions 3 and 4 (see also Figure 2.4). The

43
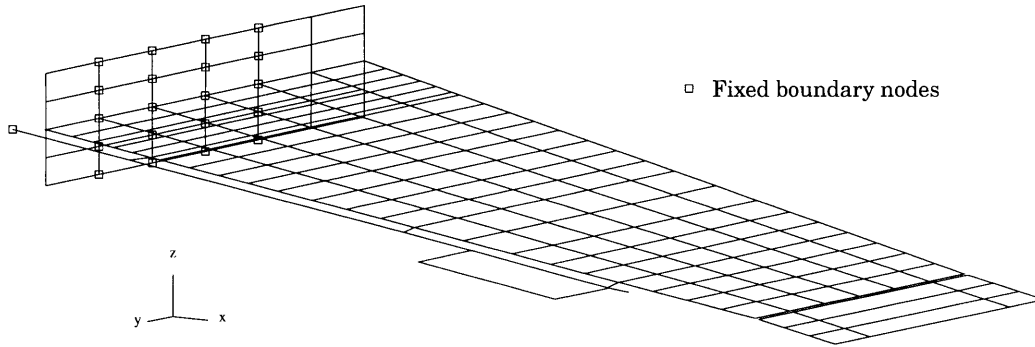
Figure 4.4: Fixed boundary node locations on the finite element mesh, viewed from above and behind the trailing edge tip

remaining plate regions, regions 5 through 11, are single-layer elements representing the aluminum testbench plate. All plate elements, whether single- or multi-layered, are 4 node orthotropic elements, and have either 5 or 6 degrees of freedom at each node, depending on whether the node intersects with another type of element or not. Fixed boundary conditions are imposed for the node points at which it is bolted to the mounting assembly. These boundary nodes are highlighted in Figure 4.5.

The GVT on the testbench is done with the flap drive and flutter stopper installed. Therefore, the FE model must include these items as well. The flutter stopper is modeled as a collection of isotropic beam elements, shown in Figure 4.5. All assemblies are explicitly included, except for the latch, magnet, and position sensor, which are included by increasing the density of the frame beam elements at those locations. Both the aft (undeployed) and forward (deployed) tungsten mass locations are modeled, and the two cases are considered as separate models from this point on. Figure 4.5 pictures both flutter stopper locations, although only one position

44
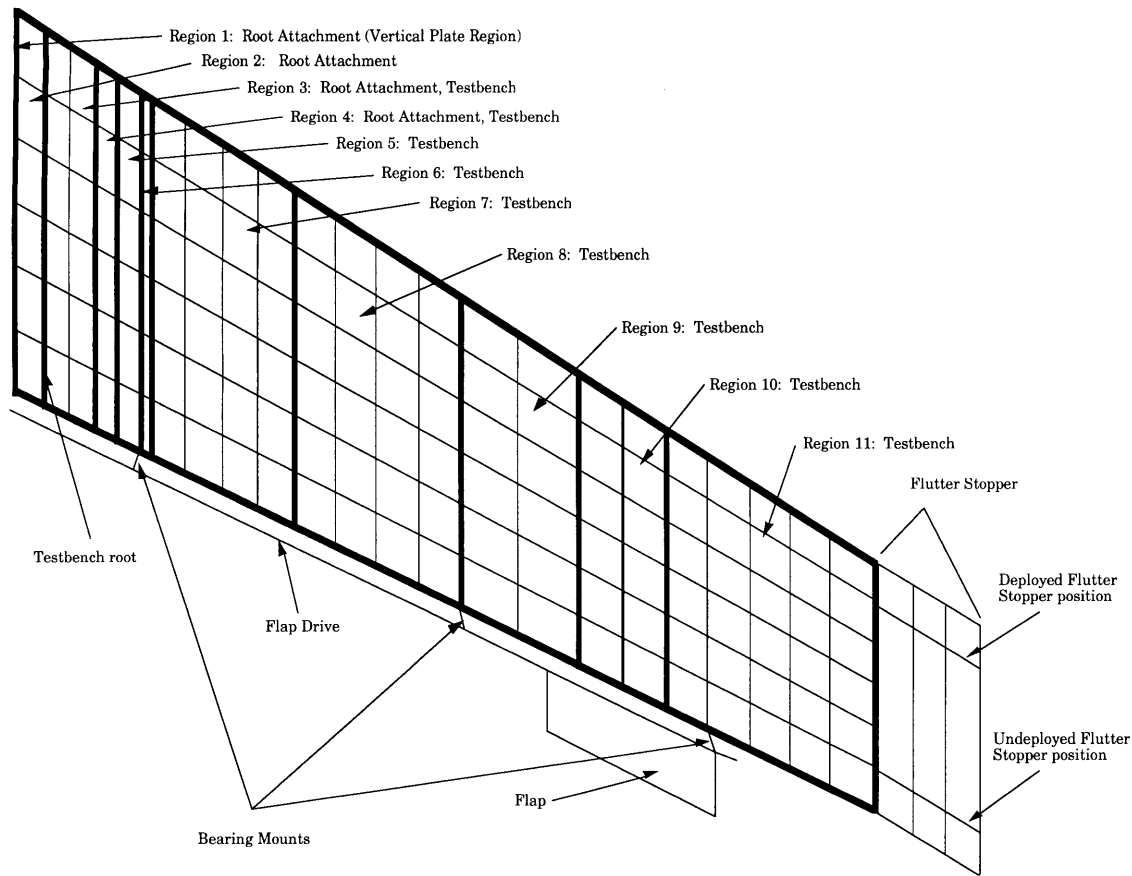
Figure 4.5: Element group regions and composition of the finite element mesh for the testbench

is used in each model. Isotropic beam elements are also used to model the flap drive, except for the flap, which is represented by a single-layered orthotropic shell. The graphite-epoxy tubes are considered homogeneous, and the material properties are consistent with the overall properties of the tubes. The spline is modeled as a single element, and no provision is given for its axial degree of freedom. The universal joints and steel rods which connect the components together are included as part of the tubes, and the weights of these pieces are added as point masses at representative node locations. Component material properties and weights for the flap drive and flutter stopper are tabulated in Appendix A.

45
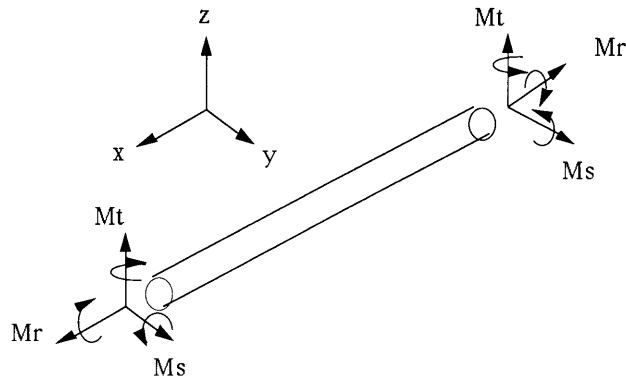
Figure 4.6: Bending degrees of freedom for beam elements

There are several places where certain degrees of freedom must be allowed along the drive shaft. The bending degrees of freedom at the universal joints are expressed by setting the bending moments in those directions on the ends of the elements to zero. In Figure 4.6, these are pictured as M_s and M_t. In addition, there must be a rotational degree of freedom between each bearing mount and the ends of the flap tubes, where the drive shaft passes through the bearings. This is achieved by creating a very short beam element between a bearing mount end node and the flap tube end nodes, as shown in Figure 4.7. This extra element translates the global deflection and rotation from the bearing mount to the drive shaft, but has zero torsional inertia to allow the shaft to rotate freely along its axis.
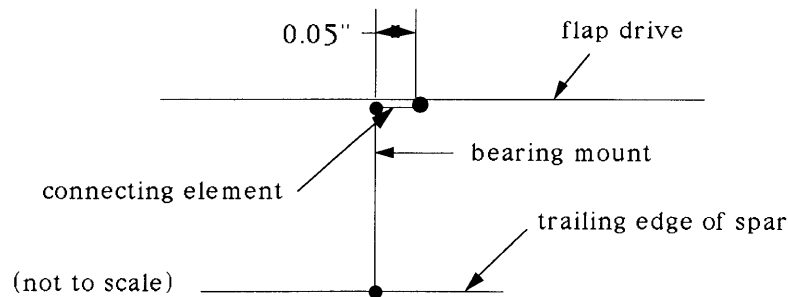
Figure 4.7: Schematic of an extra connecting element from the drive shaft to a bearing mount

The fixed boundary conditions on the flap drive are imposed by restraining all degrees of freedom at the motor end of the flap drive, in line with the end of the root attachment.

Dynamic analyses are performed for both configurations, flutter stopper deployed and undeployed. The mass matrix is consistent, and no structural damping is included. The solution algorithm solves for the 5 lowest natural frequencies, and these are output with the corresponding modeshapes. In order to compare the finite element model with the modal response, it is necessary to create a state-space representation from the finite-element model results, from which transfer functions can be extracted. From the standard spate-space system representation

$$\dot{x} = \mathbf{A}x + \mathbf{B}u$$
$$y = \mathbf{C}x + \mathbf{D}u \tag{4.1}$$

A, B, C, and D are created such that

$$\mathbf{A} = \begin{bmatrix} \mathbf{0} & \mathbf{I} \\ -\omega^2 & -2\zeta\omega \end{bmatrix} \qquad \mathbf{B} = \begin{bmatrix} \mathbf{0} \\ \Phi^T b \end{bmatrix}$$

$$\mathbf{C} = \begin{bmatrix} c_1\Phi & c_2\Phi \end{bmatrix} \qquad \mathbf{D} = \begin{bmatrix} \mathbf{0} \end{bmatrix} \tag{4.2}$$

where ω^2 is the matrix of squared natural frequencies, b is a vector of ones and zeros which selects the node at which the input occurs, and c_1 and c_2 are vectors of 1's and 0's which select the output node locations for displacement and velocity (in this case, $c_2 = [0]$). Damping must be input to the model, so ζ is set equal to 1% for each mode. The value of 1% is an acceptable approximation using the proportional viscous damping model. From this model, transfer functions can be produced between the force input location to selected output locations, or c_1 can be chosen such that all 44 locations are represented. Figure 4.8 is a FEM system response Bode plot of the FRF from the same SISO transfer function as Figure 4.3. The analytical modeshapes

47
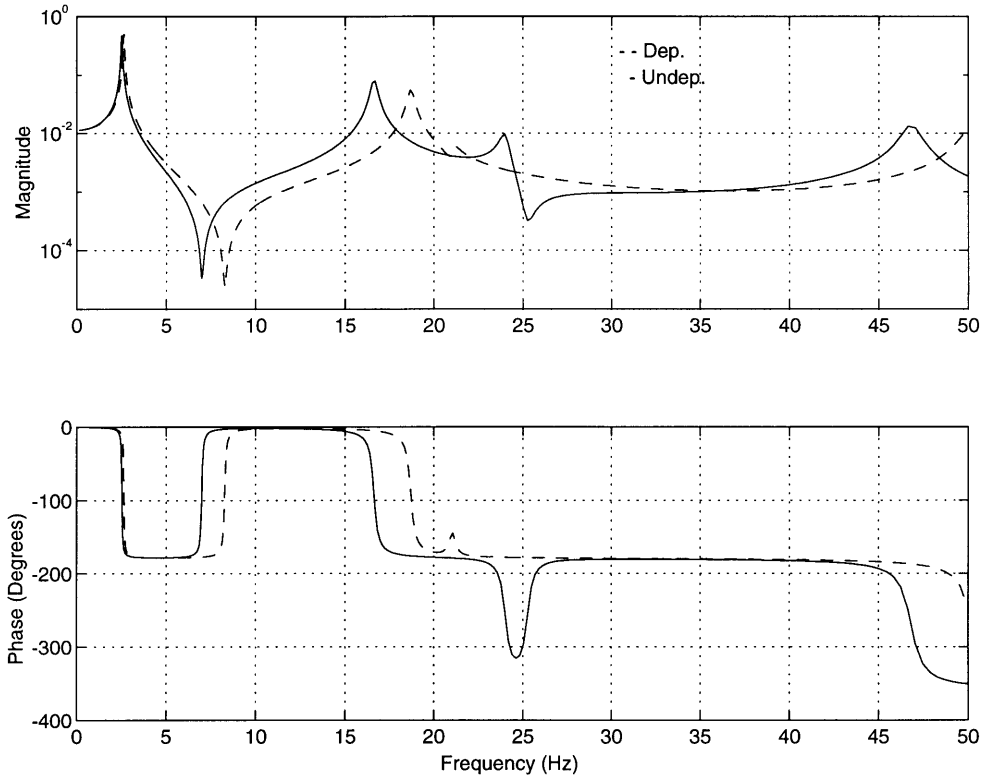
Figure 4.8: Transfer functions from the finite element model of the testbench, location 27

are shown in Appendix 4A, while the frequency response and modal characteristics are compared with the experimental results in the following section.

4.4 Testbench Model Comparison

This section contains a discussion of the two types of comparisons that are made on the modal properties of the models: qualitative comparisons, and quantitative comparisons. Qualitative methods mainly involve comparing FRFs, modeshapes, and node lines, while quantitative methods include comparing natural frequencies, as well as making a numerical evaluation of the similarity of each modeshape.

The qualitative modeshape comparisons can be made by examining the modeshapes contained in Appendix 4A in Figures 4A.1 and 4A.2. Both figures, representing modeshapes from flutter stopper deployed and undeployed models, show that the finite element model captures the modeshapes quite well.

Another comparison which addresses the quality of the correlation between modes is the comparison of node line locations, which is made in Figures 4.9(a) and 4.9(b). These figures are cartesian grid representations of
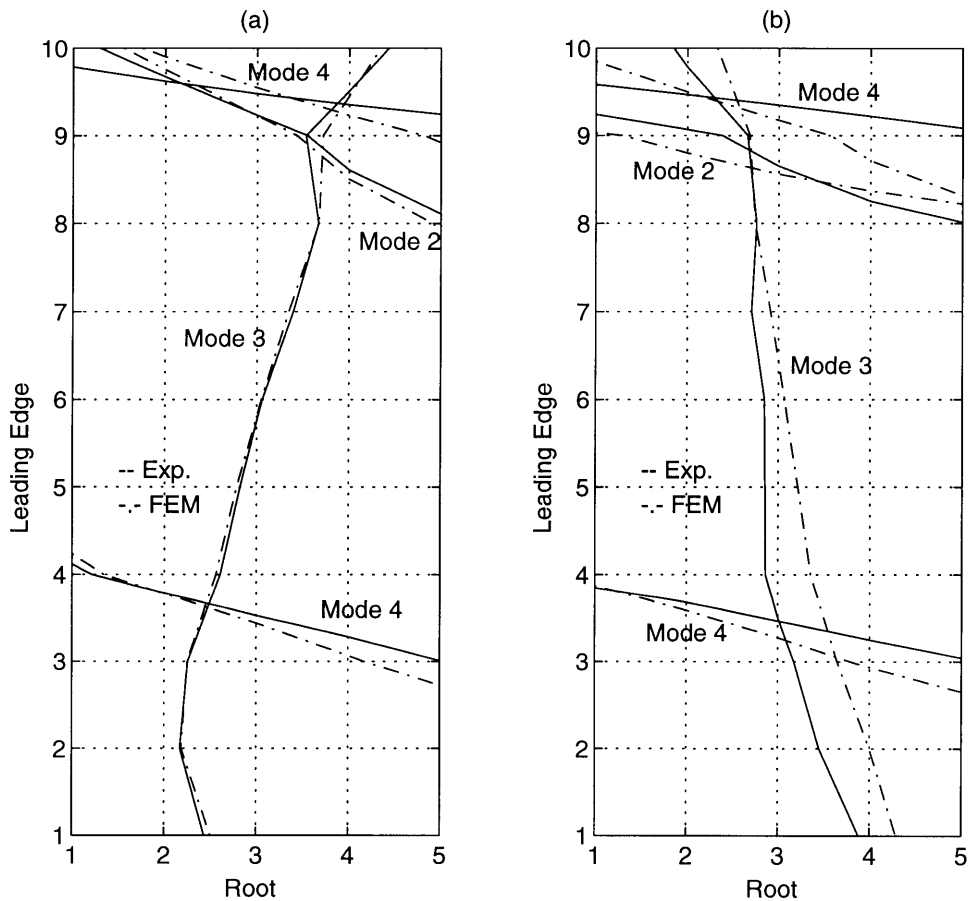
Figure 4.9: Modal contour plots on a cartesian grid for the testbench from experimental and finite element models: (a), undeployed configuration; (b), deployed configuration

49

the finite element model, where each FEM grid point at which measurements are taken is plotted on one point of the cartesian grid (see Figure 4.2). It is important to recognize that this is a skewed representation of the wing. The flap, on this grid, would be located between horizontal lines 3 and 5, and the flutter stopper is represented as the area between lines 9 and 10.

The undeployed model, pictured in Figure 4.9(a), shows good correlation for the three modes included, particularly modes 2 and 3. Obviously mode 1 cannot be compared in this way, because it has no node line. The deployed model, in 4.9(b), likewise shows good correlation, except for the third mode, in which the two models do not match exactly for the inboard section. This may be due to the stiffness of the flap drive system, which is difficult to model accurately, especially at the bearing mounts. It is easy to observe the effect that the position of the flutter stopper mass has on the modeshapes. When deployed, the node lines for modes 2 and 3 tend to become more orthogonal to the axis system of the wing. However, the finite element model does not capture this trend quite as well, and this difference is clearly seen at the bottom of Figure 4A.2.

The comparison of frequency response functions provides an accurate account of the relative response properties of the two models. From the plots, the pole and zero locations, damping, and general trends of the system can been compared. Figures 4.10(a) and 4.10(b) are FRFs from the experimental and FE models measured at location 30 on the testbench. From Figure 4.2, it can be seen that this location is outboard of the flap on the trailing edge. Both undeployed and deployed models are included for comparison.

From these two figures, the comparison of poles and zeros can be made. In both deployed and undeployed models, the residue, damping, and frequency of the first two poles and first zero are well matched. In the
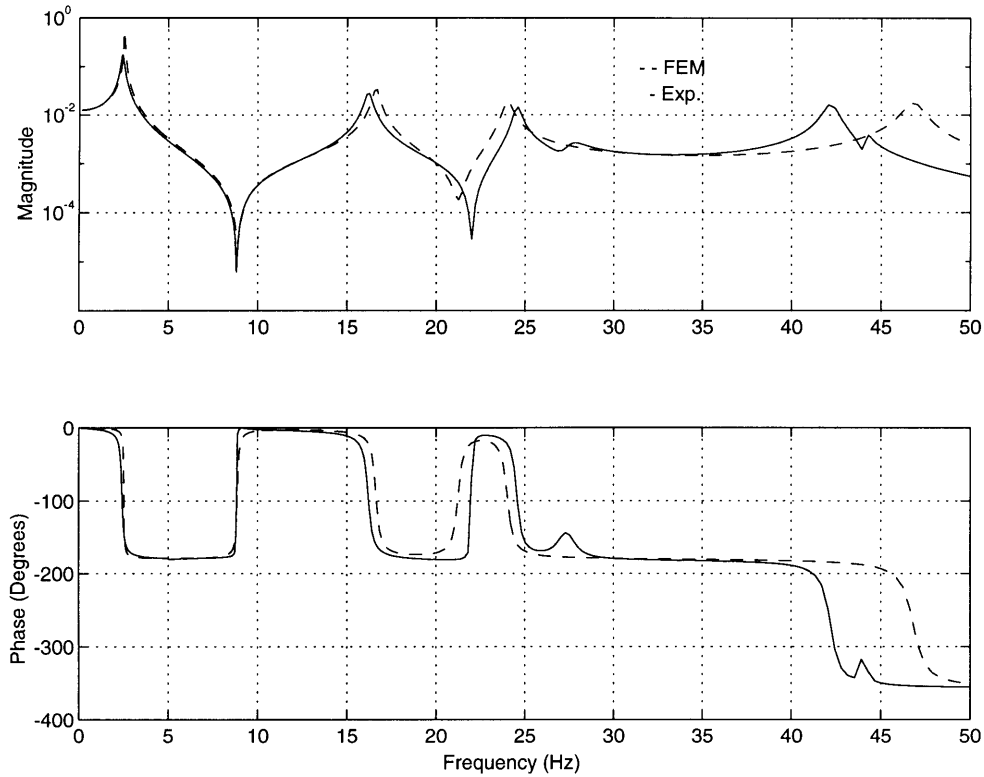
Figure 4.10(a): Transfer functions from location 4 to location 30 from experimental and finite element models for the testbench (undeployed model)

undeployed model, Figure 4.10(a), the placement of the second zero in the FEM forces the third pole to be slightly low. The experimental model includes a mode which does not appear in the finite element model, at approximately 27 Hz. This is attributed to a local rattle mode in the flap drive, due to faulty universal joints. Subsequent replacement of the universal joints removed the local mode. A similar local mode appears at 45 Hz, which is attributed to the local bending mode of the steel rods on the flutter stopper. This mode is not modeled in the finite element model, but will have negligible affect on the aeroelastic behavior of the wing.
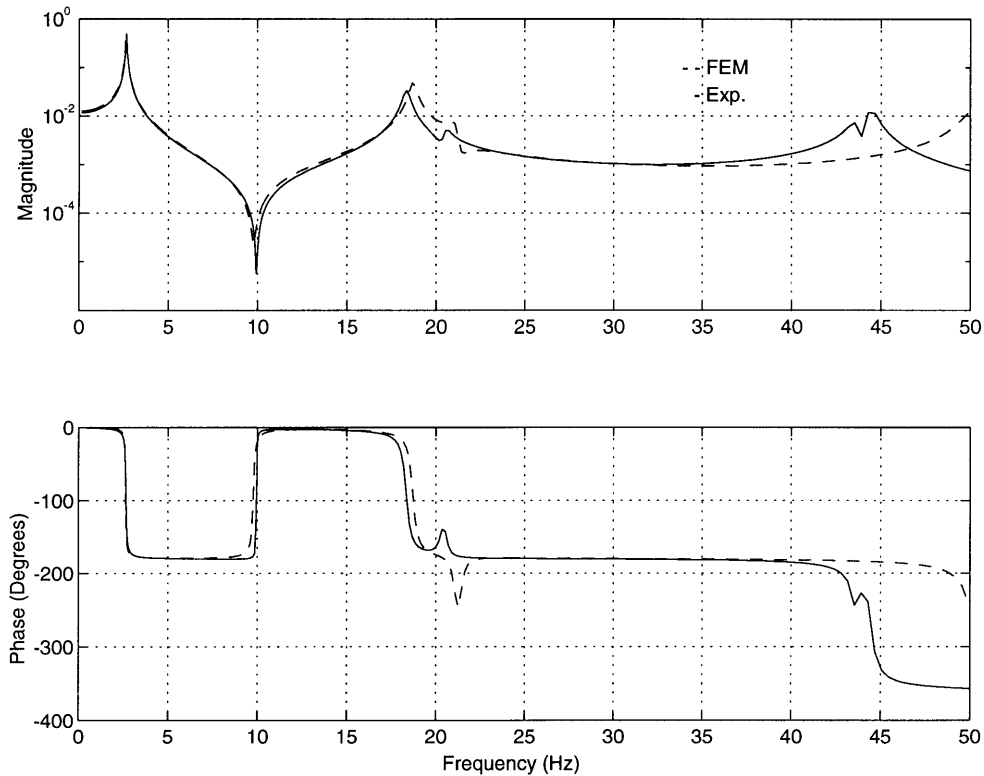
Figure 4.10(b): Transfer functions from location 4 to location 30 from experimental and finite element models for the testbench (deployed model)

There are two quantitative measures for comparison of the modal properties of the two models. The first correlation is the comparison of modal natural frequencies, tabulated in Table 4.1. Here, the frequencies are all well matched for the first 3 modes, within 5%. The difference in the fourth mode is not serious because the predicted aeroelastic behavior is a coalescence for the first two modes. The flutter stopper effects can also be seen. Deployment of the tungsten mass raises the fundamental frequency by 9.7%, and the second mode frequency by 13.2% in the experimental model.

The second quantitative measure is the Modal Assurance Criterion (MAC). It is a non-mass weighted "orthogonality" comparison between

Table 4.1: Comparison of the testbench experimental and finite element in-vacuo
natural frequencies for the undeployed and deployed configurations (in Hz)

Mode #	UD FEM	UD Exp.	% error	D FEM	D Exp.	% error
1 (1B)	2.525	2.4183	+4.41	2.639	2.6518	-0.48
2 (2B)	16.61	16.1909	+2.59	18.70	18.3307	+2.01
3 (1T)	24.01	24.5558	-2.22	21.09	20.5187	+2.78
4 (3B)	46.82	44.0931	+6.18	50.19	44.4226	+12.98

modes. Ewins [1984] describes it as a least-squares measure of the deviation of one mode from another. The definition of the MAC is

$$\text{MAC} = \frac{\left| \Phi_r^T \Phi_q \right|^2}{\Phi_r^T \Phi_r \Phi_q^T \Phi_q} \tag{4.3}$$

where Φ_r refers to modes from the experimental model and Φ_q to modes from the finite-element model. For two correlated modes, MAC values should be close to 1.0 (note that the maximum value is 1.0). For two uncorrelated modes, values should be low.

A vector argument can be made to show why the off-diagonal terms are not zero. In the case of the finite element model, the full 1416 DOF system modeshapes are orthogonal. In general, any two orthogonal vectors which are subsequently truncated are no longer orthogonal. If only the vertical displacement components of the modes are considered, any orthogonality relationship that existed previously is destroyed. Of course the testbench is really an infinite-dimensional system, and it would be impossible to capture all degrees of freedom.

Table 4.2 contains the MAC values for both undeployed and deployed models, which show correlation within 2% between the first two modes of

Table 4.2: MAC values for the testbench for the undeployed and deployed configurations

Undep.				Dep.			
.9989	-.6116	-.0626	.4626	.9989	.5309	.1155	.3416
-.6086	.9981	.1264	-.2285	.4644	.9818	-.3459	.2258
-.0907	.1582	.9955	-.1451	.1830	-.2221	.9341	-.2034
.4513	-.2046	-.1111	.9563	.3909	.1598	.0019	.9146

each model, and the third mode of the undeployed model. The diagonal values of these matrices reflect the correlation of modes as seen in the node line plots previously. The off-diagonal terms are lower but not close to zero because of the reasons cited above, and because the MAC is not mass-weighted.

The third mode discrepancy in the flutter stopper deployed configuration reflects the flap drive modeling problem discussed previously (see Figure 4.9(b)). The fourth mode discrepancy in the deployed model is also a reflection of a trend seen previously. The mode from the finite element model contains more torsion than the experimental mode, which is nearly orthogonal to the axis system of the wing (see Figures 4.9(b) and 4A.2). This may be due to the position of the tungsten mass in the finite element, deployed model. It is slightly aft of the position that it should be in, due to the approximations involved in constructing the finite element grid.

4.5 Composite Spar Modeling and Identification

This section details the application of the analysis and modeling techniques to the GVT of the composite spar. Since the composite spar experimental testing includes the aerodynamic shell, this aspect of the model

must be included as well. Some modifications are made to the actuation equipment, and to sensor and actuator locations as well.

4.5.1 Finite Element Model of the Composite Spar

This section focuses on the differences between the composite spar and testbench FE models, and the modeling of the aerodynamic shell and piezoceramic actuators, which are not part of the testbench model. Single-layered aluminum plate elements in the testbench model are multi-layered elements in the composite spar model, with material properties dependent on the element group. The FEM grid is preserved, since the testbench model was derived originally from the spar model. Figure 4.11 presents the element group regions on the finite element grid, and includes the through-thickness composition of the plate regions. One conclusion from the previous section is that the tungsten mass is not quite positioned properly in the FEM, flutter stopper deployed model. To alleviate this concern, the tungsten mass position in the deployed configuration is shifted slightly forward, which is the position shown in Figure 4.11.

The mass of the aerodynamic shell over the spar is included with the mass of the spar. The shell which extends beyond the trailing edge of the spar is modeled as point masses and inertias at the trailing edge attachment points. The shell over the flutter stopper is modeled as point masses and inertias at the three shell attachment points. In order to compensate for the chordwise stiffness of the shell sections, beams are added between leading and trailing edge attachment points for each section, except for the flutter stopper section. The effect of these beams is to raise the first torsional mode frequency by 11.6% in the undeployed model, and by 14.8% in the deployed model, to the values given in Table 4.5.
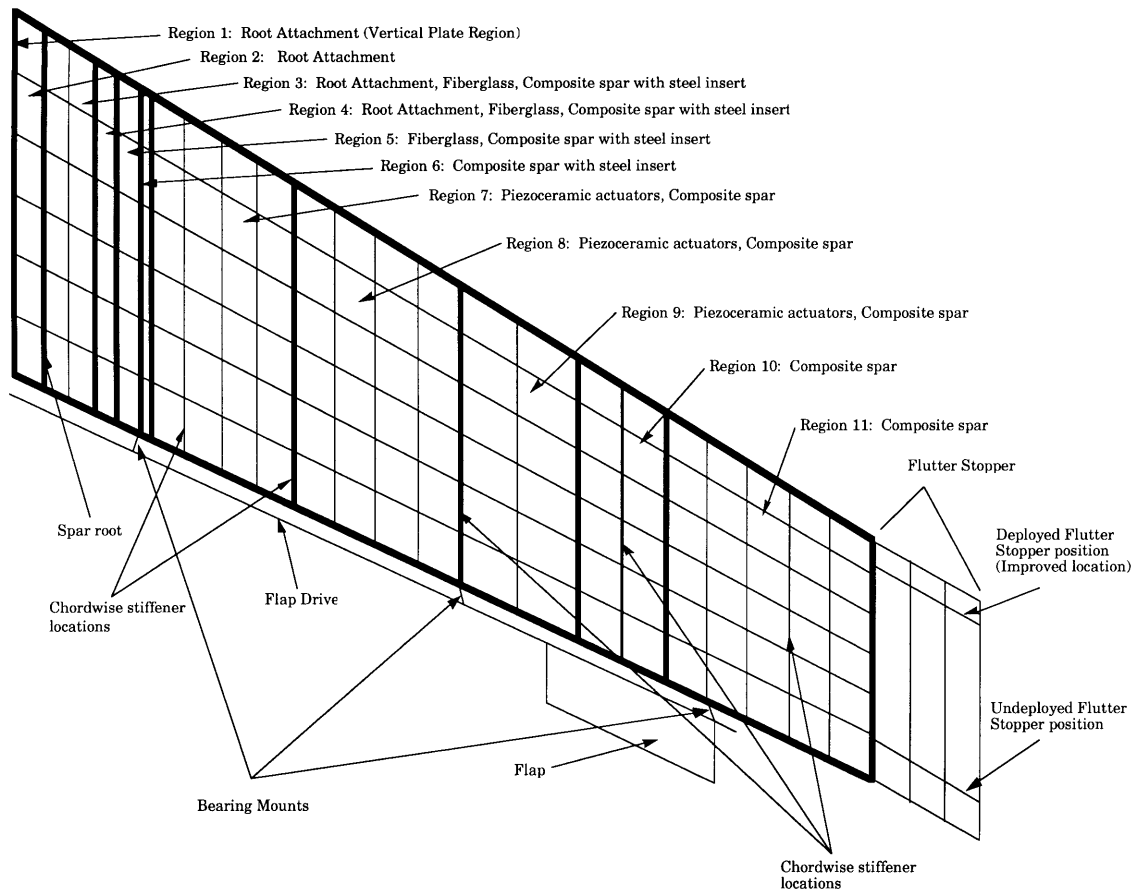
Figure 4.11: Element group regions and compositions for the composite spar finite element model

The piezoceramic actuators are modeled as solid layers of material covering the entire spar from leading edge to trailing edge over the actuation region. The actuators are not explicitly modeled as discrete devices due to the difficulty of developing the mesh necessary for that analysis. In order to retain the overall "smeared", or average, properties of the piezoceramics over the actuation region, the material stiffness, density, and thickness are artificially reduced. This approximation is valid only because the relative thickness, and effect, of the actuators is small compared to the overall structure. Lazarus and Crawley [1992] found that for thin plates with distributed actuators, where the piezoceramic material contributes the

majority of the stiffness, significant bending occurs in the regions between actuators. For a more stiff plate such as the spar, however, the discrete nature of the actuators is not as important in the stiffness model.

4.5.2 Experimental Model Identification of the Composite Spar

In order to gather the experimental FRFs on the composite spar model, the spar is mounted into the root attachment and mounting assembly. The shaker is mounted on a stand which effectively eliminates the need for a long stinger to reach from the shaker to the wing. Figure 4.12 shows how a short section of tube is connected through a single wire moment release to the load cell, which is mounted immediately adjacent to the spar. The load cell is connected to a small aluminum pad mounted to the spar surface with epoxy. The entire stinger length, including load cell, is approximately 5 inches. Location 40, which is the grid point closest to the trailing edge tip, is chosen as the actuation node (see Figure 4.2).

Data taken for the composite spar is concentrated over the range from zero to 50 Hz, divided into 4096 points. The data below 2 Hz is again
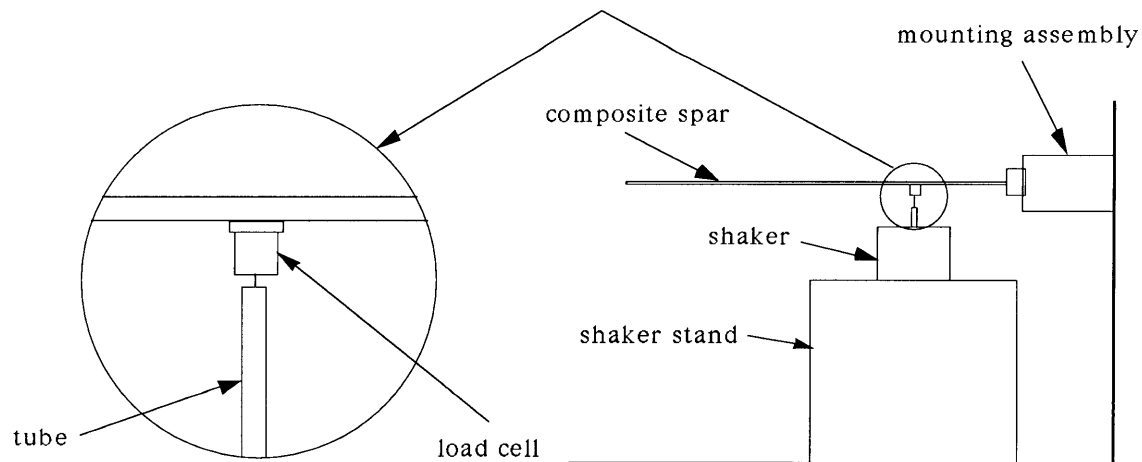
Figure 4.12: Experimental test setup for the composite spar

truncated due to the accelerometer charge amplifier. Measurements are taken at the same 44 locations on the finite element mesh from Figure 4.2.

4.6 Composite Spar Model Comparison

4.6.1 Model Comparison Without the Aerodynamic Shell

Because the shell complicates the dynamics of the model, data is first taken without the shell in an attempt to validate the dynamics of the spar itself. The quantitative comparisons between measured and FE models are located in Tables 4.3 and 4.4, which tabulate the modal frequencies and the MAC matrices, respectively. Figures 4.13 and 4.14 include the nodal contour plots and the Bode frequency response plots of the two models. The modeshapes are pictured in Appendix 4B.

The frequencies tabulated in Table 4.3 show that the finite element model is correlated to within 4% of the experimental model, except for the second mode in the flutter stopper deployed case. The FE model is nearly 9% high for this modal frequency. The MAC values in Table 4.4 are all within approximately 5%, except for the fourth mode of the deployed configuration. This value deviates widely, and the reason for this will be discussed later.

Table 4.3: Comparison of composite spar experimental and finite element in-vacuo natural frequencies for the undeployed and deployed configurations without the aerodynamic shell (in Hz)

Mode #	UD FEM	UD Exp.	% error	D FEM	D Exp.	% error
1 (1B)	2.801	2.6987	3.79	3.156	3.0932	2.03
2 (1T)	16.09	16.2117	-0.75	13.43	12.3429	8.81
3 (2B)	21.96	21.6053	1.64	23.21	22.4514	3.38
4 (2T)	45.05	46.7812	-3.70	45.13	45.5220	-0.86

58

Table 4.4: MAC values for the composite spar in the undeployed and deployed
configurations without the aerodynamic shell

Undep.				Dep.			
.9995	-.6617	.4661	.0475	.9995	-.2487	.5090	-.3546
-.6249	.9844	-.3975	-.2560	-.0382	.9489	.4302	-.1839
.3916	-.2344	.9778	.2979	.3845	.3647	.9607	-.3851
-.0396	-.1165	.2580	.9698	-.2118	-.2925	-.5369	.8515

The classification of the fourth mode in Table 4.3 as the second torsional mode is somewhat arbitrary, due to the effect of geometric and fiber sweep on the wing [Jensen and Crawley, 1984]. For example, for plates with geometric and/or fiber sweep, the second and third modes start, at one extreme, as the second bending and first torsional modes, and then rotate, as the fiber sweep angles increase, to torsion and bending, respectively. For the present case, with both geometric and fiber sweep, the fourth mode exhibits characteristics of both bending and torsion. However, the overall tendency of the mode is more towards torsional motion than bending motion, as can be seen in Appendix 4B.

In Figure 4.13, node lines of the undeployed and deployed flutter stopper models are plotted on the cartesian grid of Figure 4.9. The node lines have been divided into two separate plots each for undeployed and deployed cases for clarity. The most striking characteristic of this figure is the change in the nature of the second and third modes as the flutter stopper is deployed. While in the undeployed configuration, the modes both contain characteristics of bending and torsion. In the deployed configuration, the modes are more clearly bending or torsion individually.

59
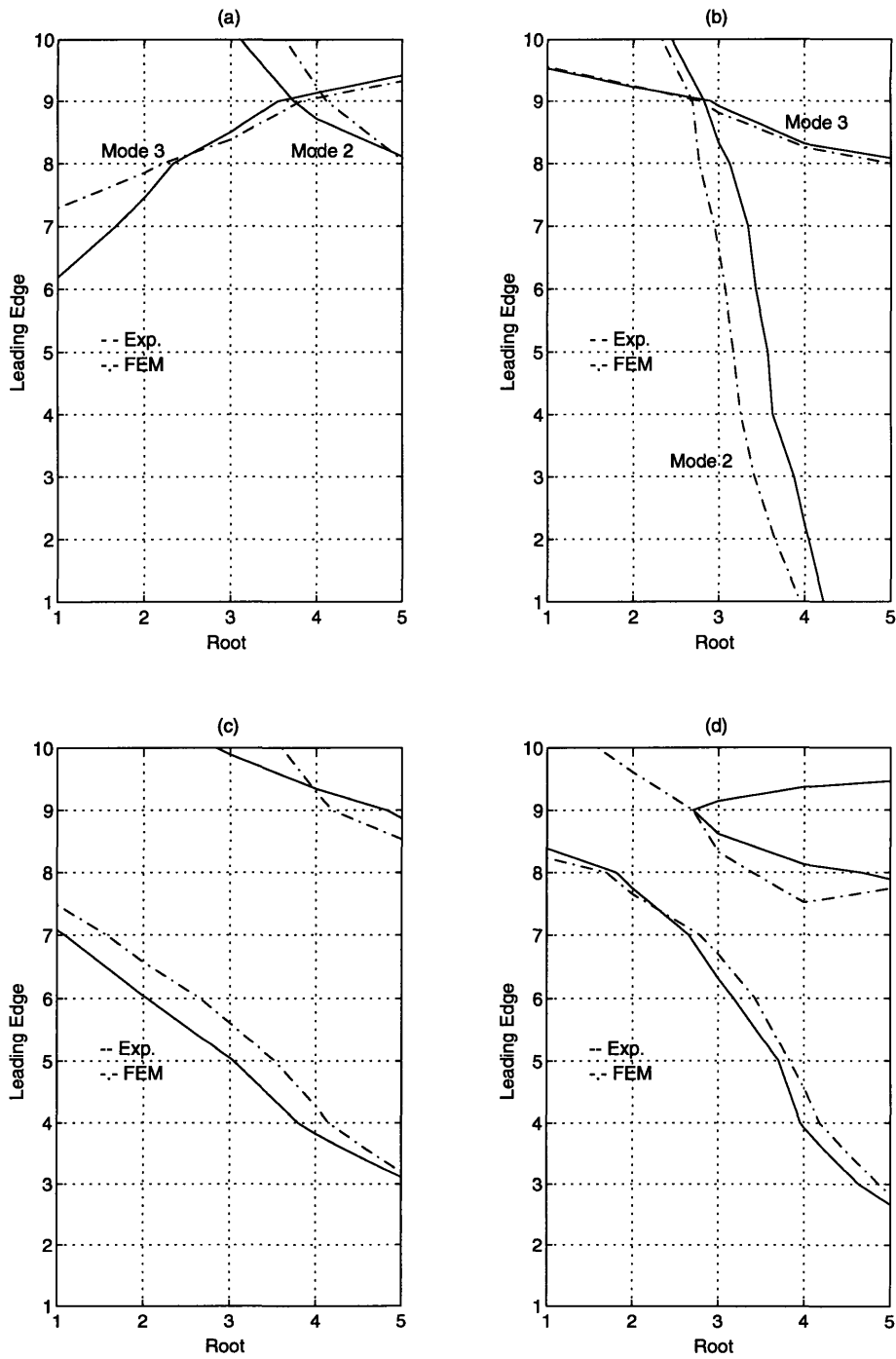
Figure 4.13: Modal contour plots on a cartesian grid for the composite spar without the shell from experimental and finite element models (a), undeployed configuration modes 2 and 3; (b), deployed configuration modes 2 and 3; (c), undeployed configuration mode 4; (d), deployed configuration mode 4

The deployed flutter stopper model fourth mode deviates more than the others, and the reason for this can be seen at the bottom of the deployed modeshapes in Appendix 4B. The outboard trailing edge tip of the experimental model does not dip down as much as might be expected. The flutter stopper is a comparatively rigid body, and should not twist as it does in this mode. This may be due to the accelerometer not being placed correctly at the tip, perhaps on the slanted frame which would cause the measurement of acceleration in some skewed coordinate system. This deviation is also apparent in Figure 4.13(d), and in Table 4.4.

Figure 4.14(a) pictures the undeployed TFs from experimental and finite element models. The plots are quite similar below about 30 Hz, which

Figure 4.14(a): Transfer functions from location 40 to location 30 from experimental and finite element models for the wing without the shell (undeployed model)

61
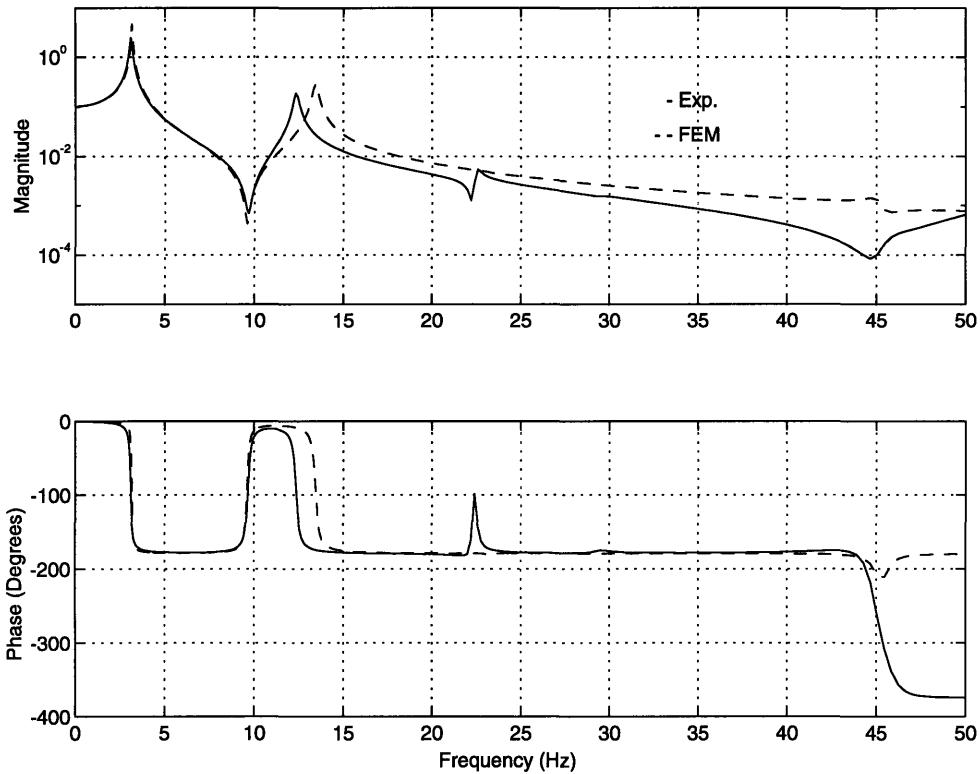
Figure 4.14(b): Transfer functions from location 40 to location 30 from experimental and
finite element models for the wing without the shell (deployed model)

is the aeroelastic region of interest. The TF of the deployed model, shown in
Figure 4.14(b), is much harder to compare. In the finite element model,
location 30 is very close to the node lines of modes 2 and 4, and the actuator
node, location 40, is very close to the node line of mode 3. The effect of this is
that modes 2 through 4 are practically unobservable in the given transfer
function. The experimental model shows modes 2, 3, and 4 (which is above 50
Hz for this TF), because the node lines are further from the corresponding
node locations.

4.6.2 Model Comparison With the Aerodynamic Shell

After the data is correlated for the spar without the shell, the shell is added and this model re-identified. In order to actuate the spar directly, a node point along the edge of a shell section is chosen, so that a stinger can be placed between sections. Location 25 is chosen as the actuation point for this reason. Because the shell's surface is sloped, the accelerometer is mounted to the shell with small plastic wedges, which allow the measurement of vertical acceleration. As a reference, a weight breakdown of the major wing components is tabulated in Table 4.5 In addition, extra modal data is measured at points on the shell behind the trailing edge of the spar, and along the leading edge of the spar. While not useful for the present analysis, this information helps build a more complete modal model for future aeroelastic analyses.

The comparison between the measured and finite element models is harder to make, due to the effects of taking measurements on the shell itself. Because the shell sections are only attached to the spar at a single spanwise location, measurements anywhere on the shell will only reflect the response of the spar at the attachments. Modal information which occurs between shell attachment locations is lost. The finite element model has no explicitly defined shell, so transfer functions derived from the FEM correspond to

Table 4.5: Weight breakdown of major components of the wing model

Component	Weight
Composite spar (includes piezos)	11.44 lbs (50.96 N)
Flap drive system	1.76 lbs (7.84 N)
Flutter Stopper	6.44 lbs (28.69 N)
Aerodynamic Shell	9.36 lbs (41.69 N)

Table 4.6: Comparison of experimental and finite element in-vacuo natural frequencies for the composite spar with the aerodynamic shell (in Hz)

Mode #	UD FEM	UD Exp.	% error	D FEM	D Exp.	% error
1 (1B)	2.447	2.5132	-2.63	2.641	2.6656	-0.92
2 (1T)	12.46	13.4479	-7.34	11.88	12.2218	-2.80
3 (2B)	17.32	17.6667	-1.96	17.14	16.9049	1.39
4 (2T)	35.58	36.5844	-2.74	35.74	35.3775	1.02
5 (3B)	47.63	42.6385	11.71	47.68	41.8963	13.80

points on the spar itself. The frequency comparison is a better measure of the correlation for this reason.

The flutter stopper effects can be seen in Table 4.6, which is a comparison of the modal frequencies. The first bending mode frequency increases by 6.1% as the mass deploys, and the first torsional mode decreases by 9.1%. From this information, it is impossible to predict what the flutter mechanism will be, and at what frequency. If this were the only gauge by which predictions could be made, then flutter would be predicted to occur at a lower flight speed for the deployed model as compared to the undeployed model, because there is a smaller ratio between the first two modes in the deployed model. Fortunately, the flutter mechanism is dominated by the position of the chordwise CG relative to the elastic axis, and not simply by the spacing of the modes. The only method of determining the flutter speeds is to do a detailed aeroelastic flutter prediction, which is presented in Appendix B.

From Table 4.6, the frequencies from both configurations are within 3% through the first 4 modes, except for the second mode of the flutter stopper undeployed model. This can also be seen in Figures 4.15(a) and
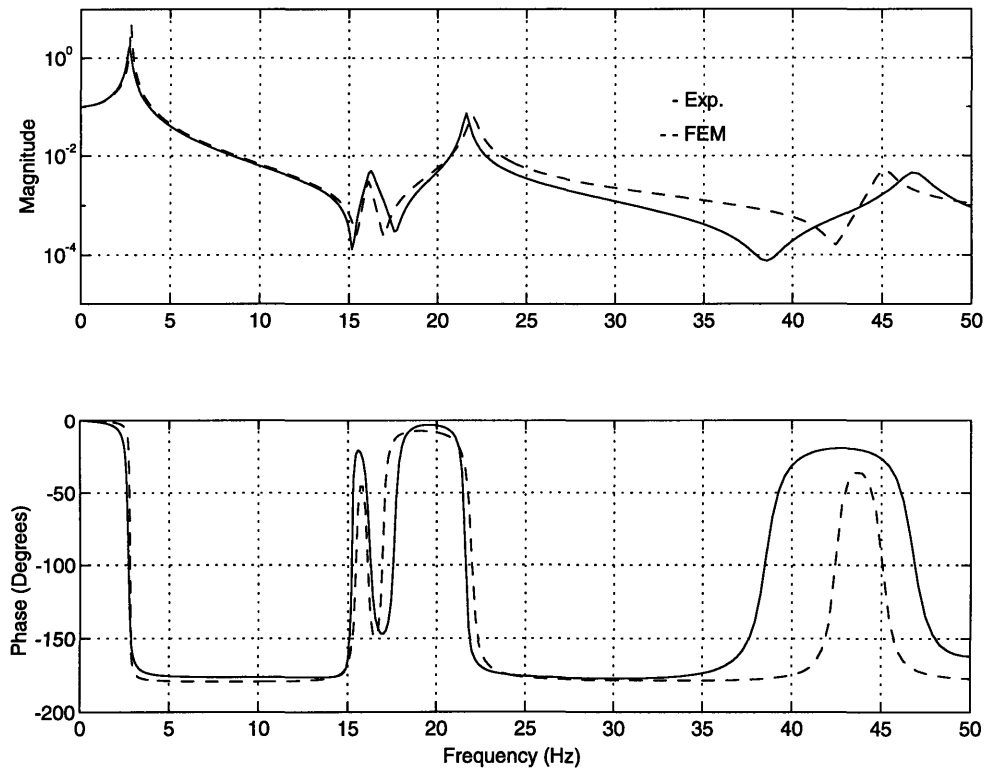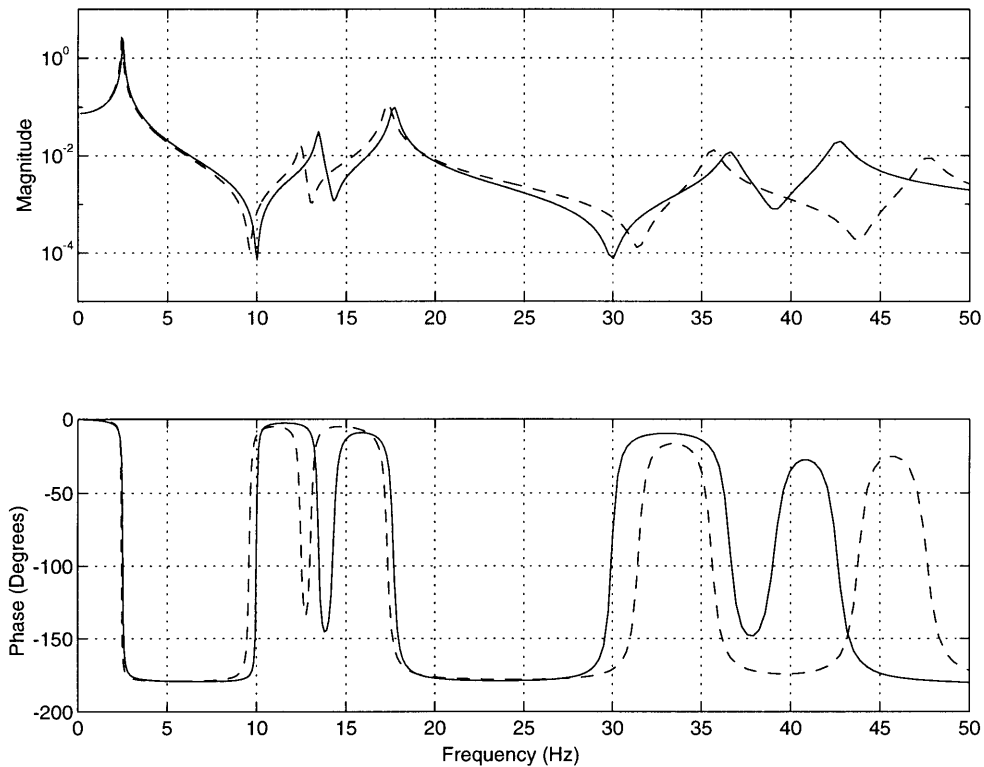
Figure 4.15(a): Transfer functions from location 25 to location 30 from experimental and finite element models for the wing with the shell (undeployed model)

4.15(b), which are the FEM and experimental FRF Bode plots for the undeployed and deployed flutter stopper configurations. The two figures show that the overall system response is well correlated below about 30 Hz. The fourth pole is captured, however the influence of the fifth mode pushes the fourth zero closer to the fourth pole, which changes the response. Table 4.7, however, reflects the problems in comparing the FEM and experimental models. The first two values of the MAC for the undeployed model, and the first three for the deployed model, are good, but the quality of the correlation diminishes rapidly thereafter.
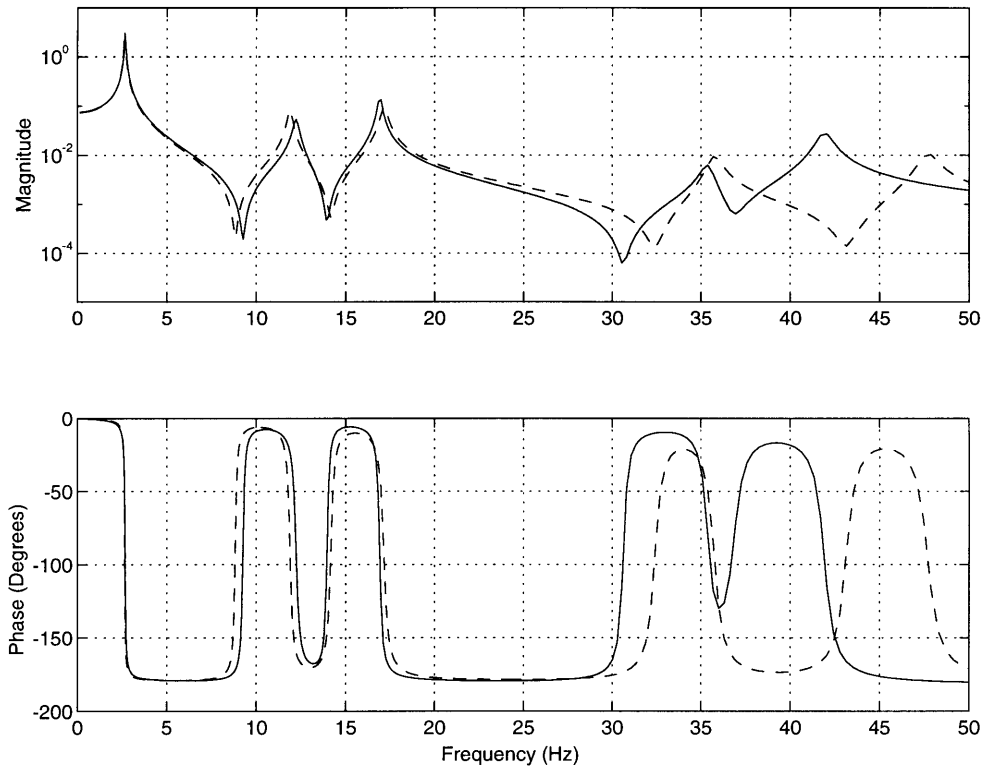
Figure 4.15(b): Transfer functions from location 25 to location 30 from experimental and finite element models for the wing with the shell (deployed model)

Table 4.7: MAC values for the composite spar with the aerodynamic shell for undeployed and deployed cases

Und.					Dep.				
.9935	-.6392	.4413	-.0089	-.6137	.9927	.0739	.5356	-.2385	-.6335
-.5699	.9805	-.4123	.2743	.5369	.0234	.9733	-.3606	.2068	.1930
.2545	-.0861	.9050	-.2418	-.0887	.5152	-.3055	.9886	-.4178	-.4125
-.0989	.1100	-.1807	.8305	.0708	-.4039	.1361	-.3675	.8083	.3402
-.5852	.5152	-.4829	-.0506	.8731	-.5764	.1333	-.5129	-.1038	.8768

66

The figures in Appendix 4C graphically illustrate the problems associated with the discontinuous shell. These are the modeshape plots of the deployed and undeployed configurations. As can be seen in Figures 4C.1 and 4C.2, the first three modeshapes in both cases are quite similar in appearance. There is very little curvature in the structure for these modes. The shell sections stay in line with each other, for the most part. In contrast, the fourth and fifth modes have a significant amount of curvature, and the shell sections no longer line up with each other. This is especially visible in mode 4 of both configurations. However, besides the discontinuity of the modes, the general shape of each mode is preserved between the experimental and FE models.

Figures 4.16(a) through (d) plot the node line locations of the experimental and finite element modeshapes on the cartesian grid. In 4.16(a) and 4.16(b), the mode lines of the second and third modes are fairly good, except for the third mode in the undeployed configuration. However, Figures 4.16(c) and 4.16(d) paint an entirely different picture. The contours of the fourth mode in both cases are vastly different on the outboard half of the wing. However, by inspection of mode 4 in these two plots, similarities arise which shed light on the problem. In both cases, the experimental node line closest to the wingtip appears to span from one FEM node line to another. This, and the fact that the two experimental node lines near the tip seem to delineate a saddle region, especially in 4.16(c), suggests that the experimental model is lower than the FE model.

On visual inspection of the values for the modeshapes of these two modes, this is in fact the case. The experimental modeshape values consistently are slightly below the FEM modeshapes for the fourth mode. This is especially the case for the points near the tip of the wing. This

67
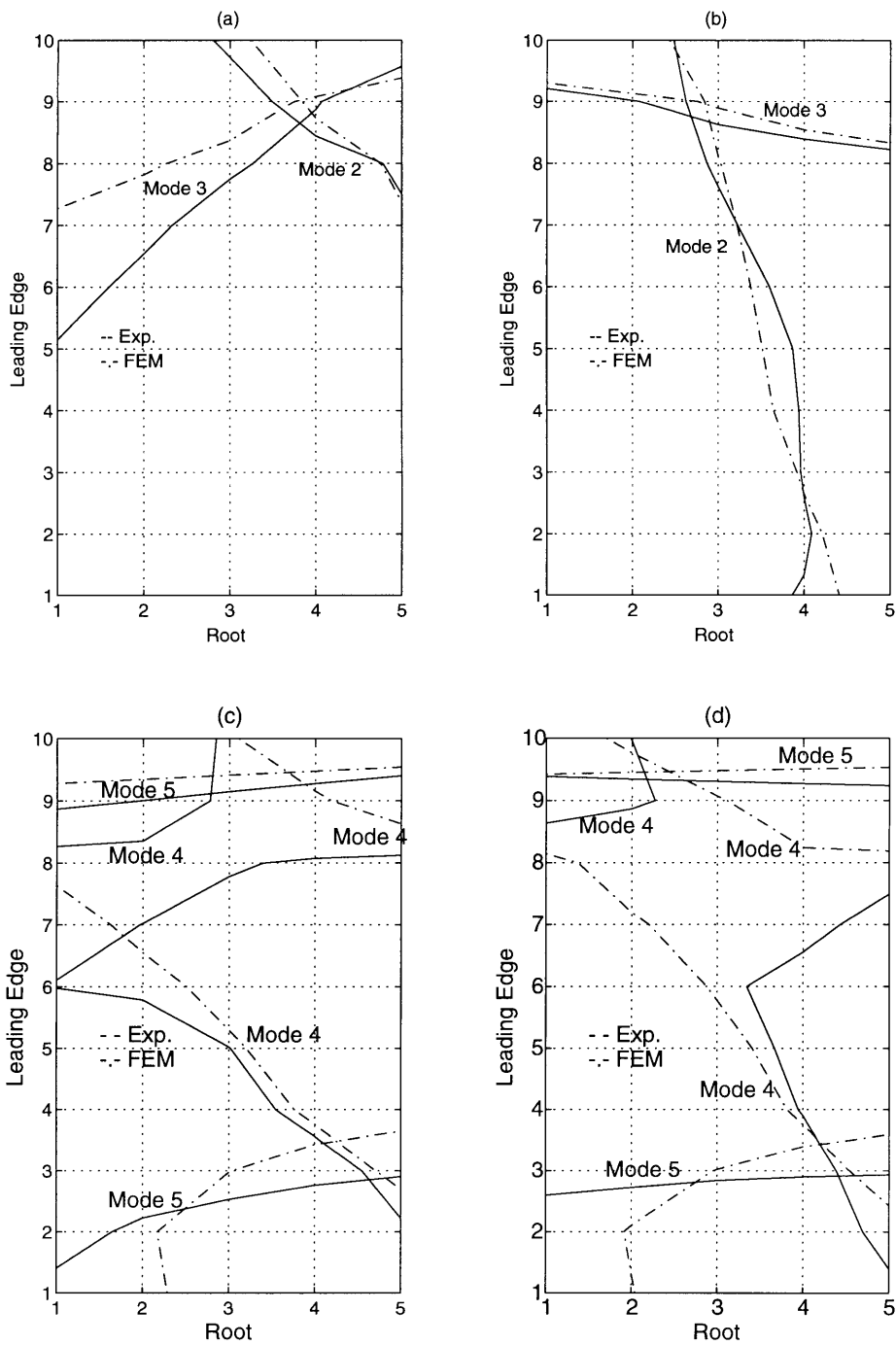
Figure 4.16: Modal contour plots on a cartesian grid for the composite spar with the shell from experimental and finite element models; (a), undeployed configuration modes 2 and 3; (b), deployed configuration modes 2 and 3; (c), undeployed configuration mode 4; (d), deployed configuration mode 4

phenomenon is due to the fact that the experimental model sags under its own weight, and the modeshapes reflect this sag. The finite element model, on the other hand, does not include this gravity effect. The difference is that the finite element model solution is executed on the structure as it exists in a vacuum. This is not to say that gravity is not included in the model. To remedy this, the solution must be done in two parts: first, a static solution with gravity loading is done to find the model's equilibrium position, and then the dynamic solution is completed on the deformed model.
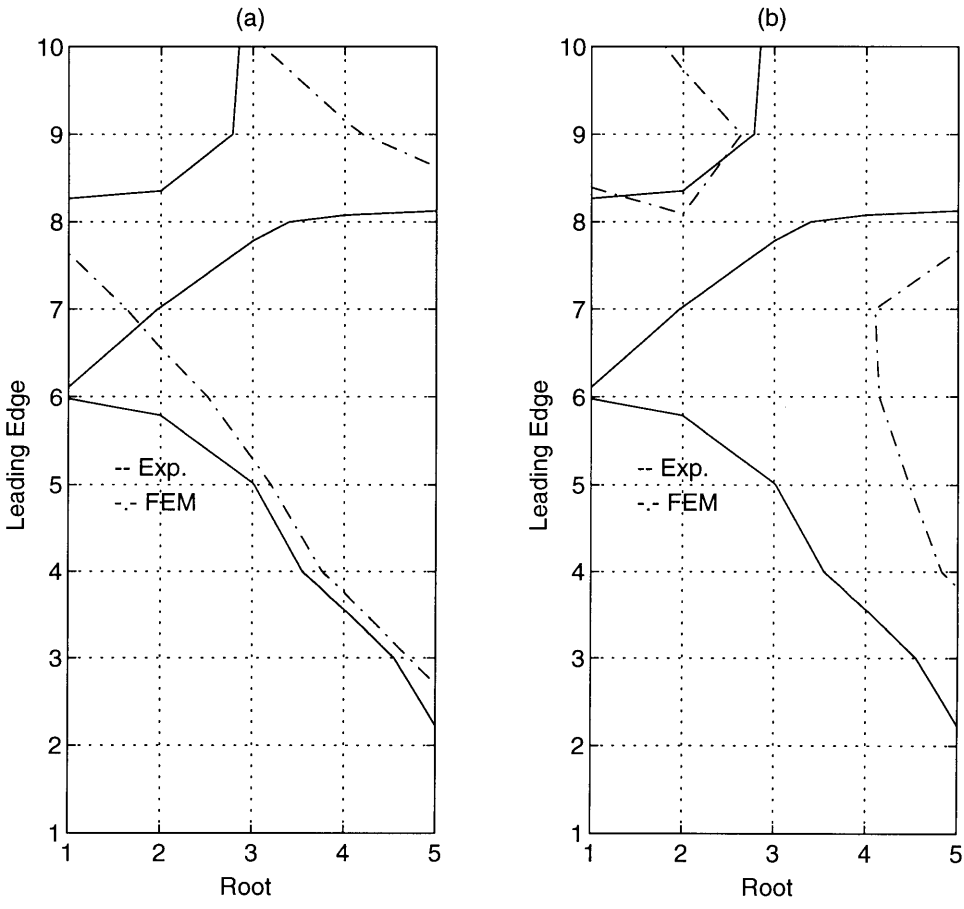
Figure 4.17: Mode 4 node line contour plots of the undeployed flutter stopper experimental and finite element models for the composite spar with the shell; (a), original models; (b), original experimental model, FE model with artificial zero-order structural sag

Figures 4.17(a) and (b) show a graphic picture of what happens when the finite element model includes sag. These are contour plots of the experimental and finite element fourth mode node lines for the flutter stopper undeployed case only. In 4.17(a), the original node lines are plotted, exactly as they are in Figure 4.16. In 4.17(b), however, the FEM modeshapes have been artificially reduced to simulate this sag. The sag of the structure can be described by a fourth order polynomial, however for this simple example a constant value is chosen. While the new node lines do not exactly match the experimental contours, the general trends do appear. The result is clear: the experimental and FEM modeshapes, while differing in details, are similar in the general shape of the mode. This method can also be used to match the fifth mode node lines at the wing root.

This trend was not visible in any of the other models because they did not include the shell. The addition of the shell increases the structure's weight by 48% (see Table 4.5). The first three modes of the models which include the shell are not as affected because the slopes of these modeshapes are very shallow, and so a vertical displacement of the entire modeshape does not affect the node line location as much.

Appendix 4A: Testbench Modeshapes

Mode 1 - FEM

Mode 1 - Exper.

Mode 2 - FEM

Mode 2 - Exper.

Mode 3 - FEM

Mode 3 - Exper.

Mode 4 - FEM

Mode 4 - Exper.
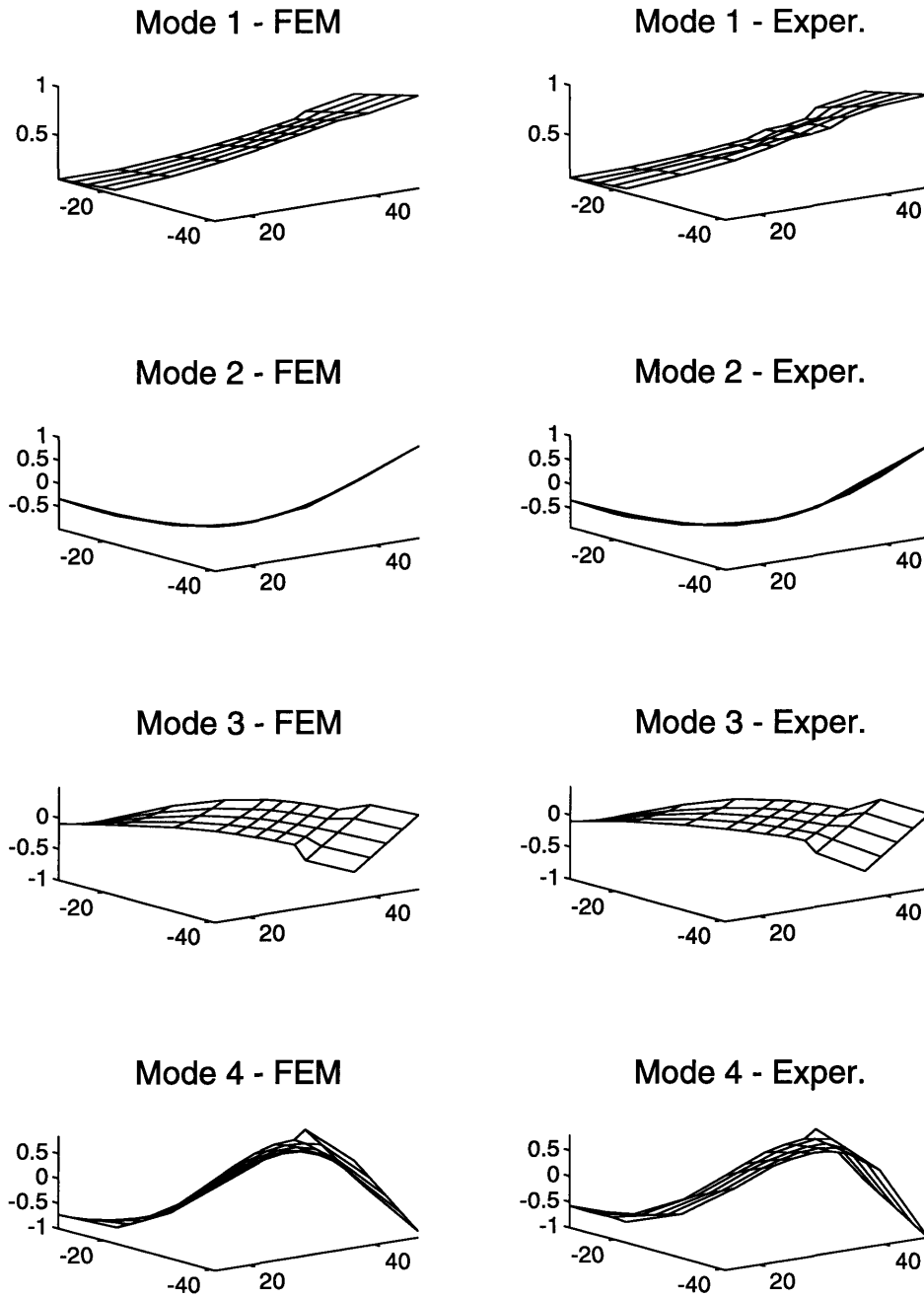
Figure 4A.1: Undeployed modeshapes for the testbench for experimental and finite element models (trailing edge out, root on the left)
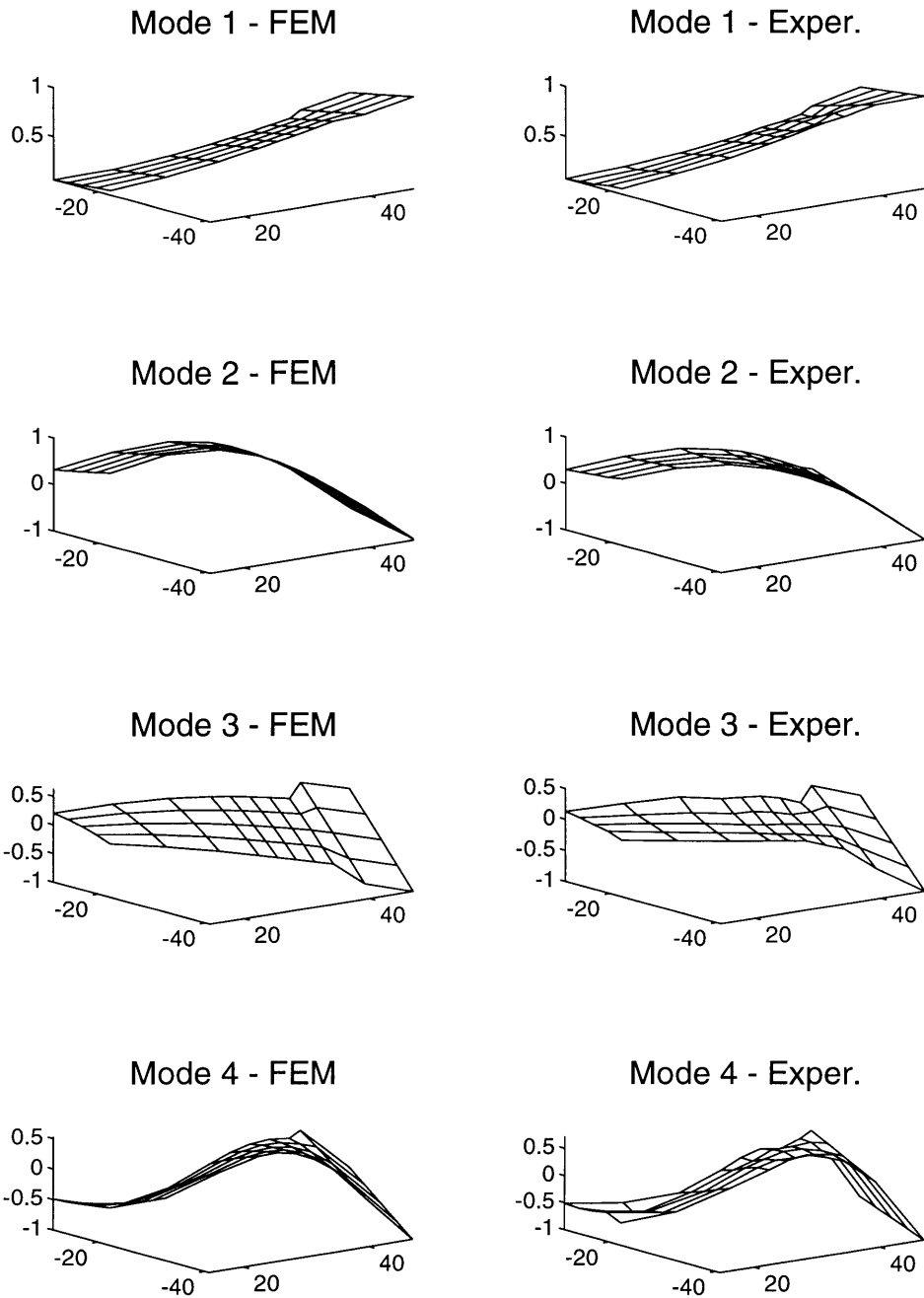
Figure 4A.2: Deployed modeshapes for the testbench for experimental and finite element models (trailing edge out, root on the left)

Appendix 4B: Spar Modeshapes, No Shell

Mode 1 - FEM

Mode 1 - Exper.

Mode 2 - FEM

Mode 2 - Exper.

Mode 3 - FEM

Mode 3 - Exper.

Mode 4 - FEM

Mode 4 - Exper.
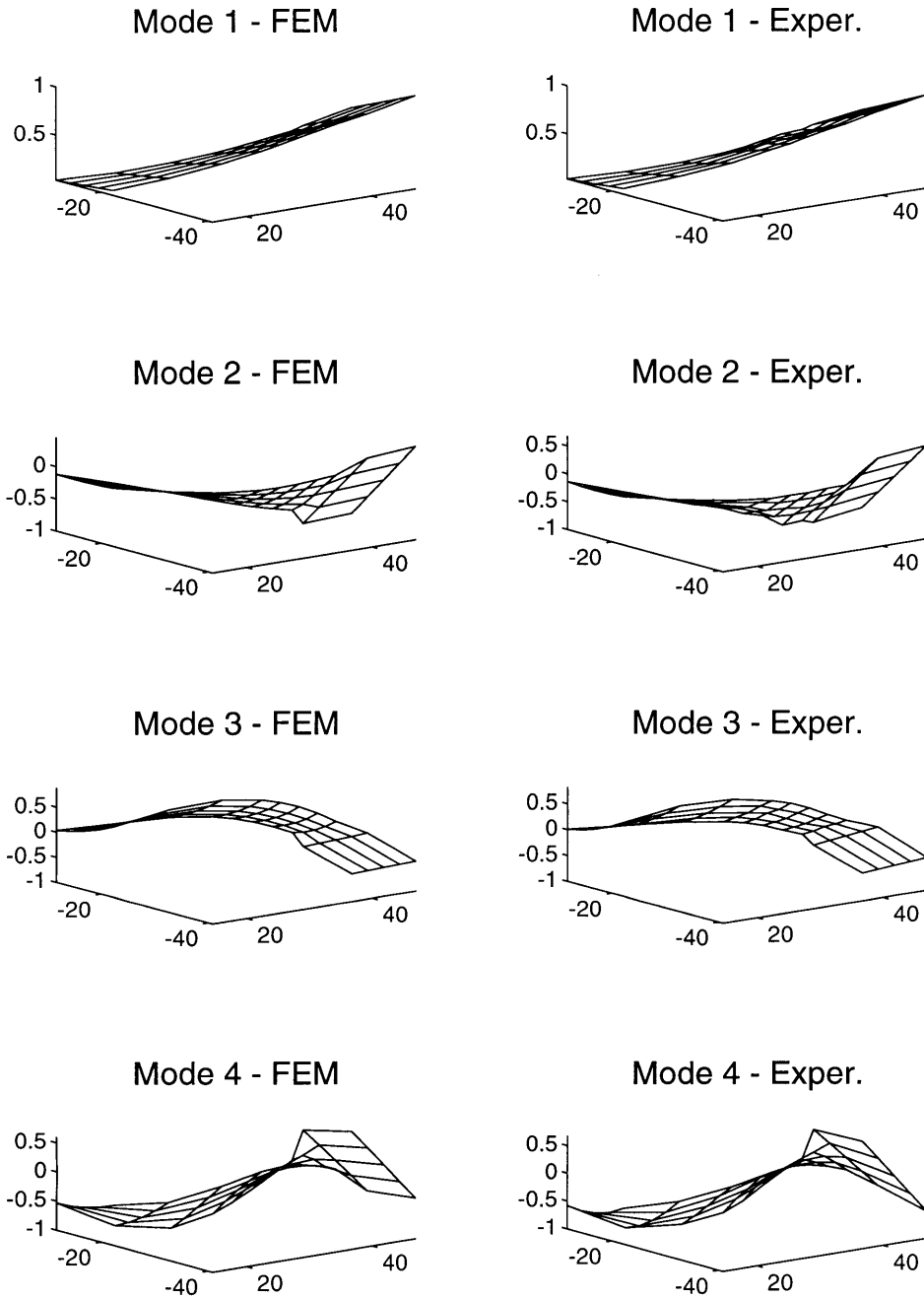
Figure 4B.1: Undeployed modeshapes for the spar without the shell for experimental and finite element models (trailing edge out, root on the left)

Mode 1 - FEM

Mode 1 - Exper.

Mode 2 - FEM

Mode 2 - Exper.

Mode 3 - FEM

Mode 3 - Exper.

Mode 4 - FEM

Mode 4 - Exper.
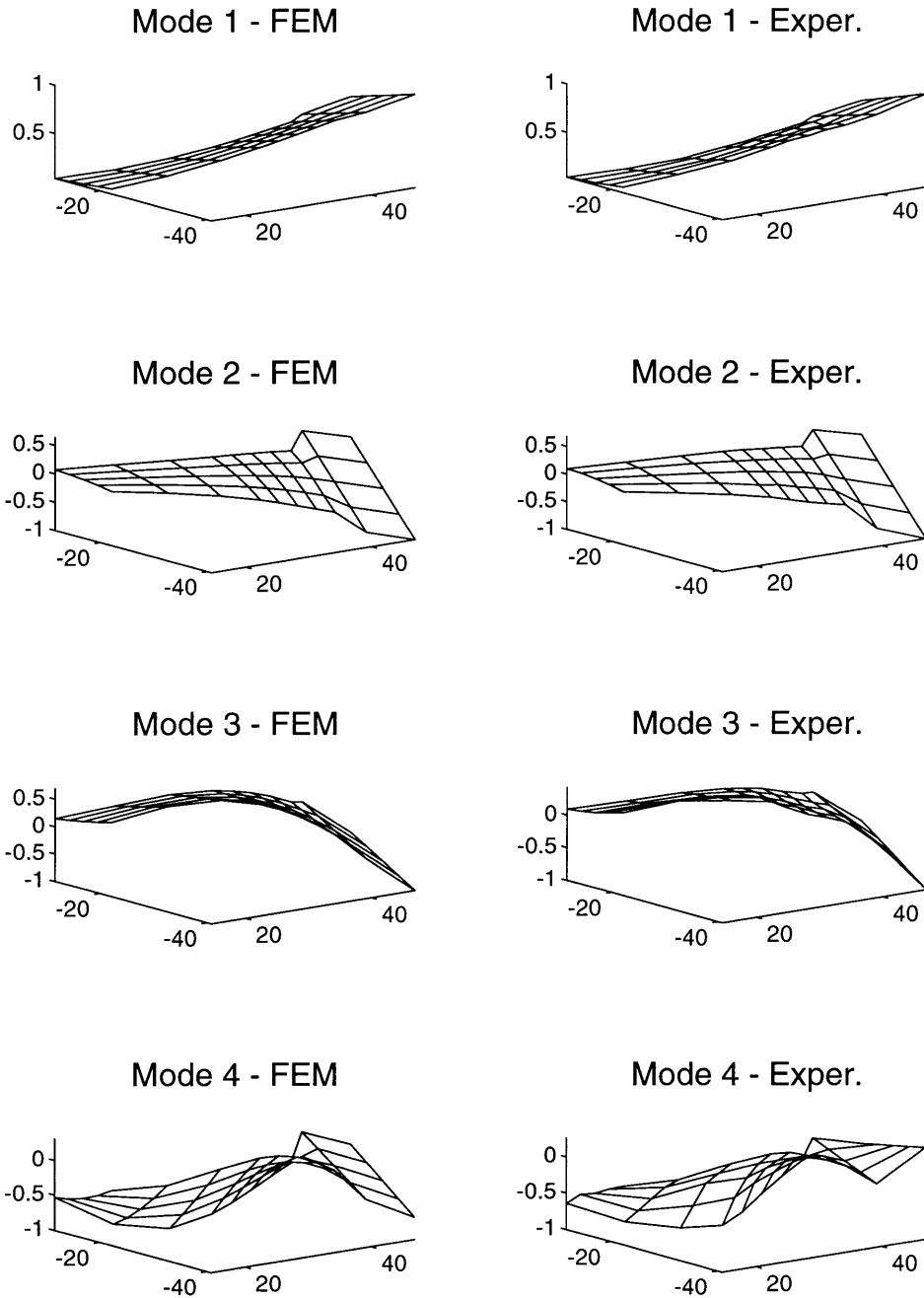
Figure 4B.2: Deployed modeshapes for the spar without the shell for experimental and finite element models (trailing edge out, root on the left)

74

Appendix 4C: Spar Modeshapes, With Shell
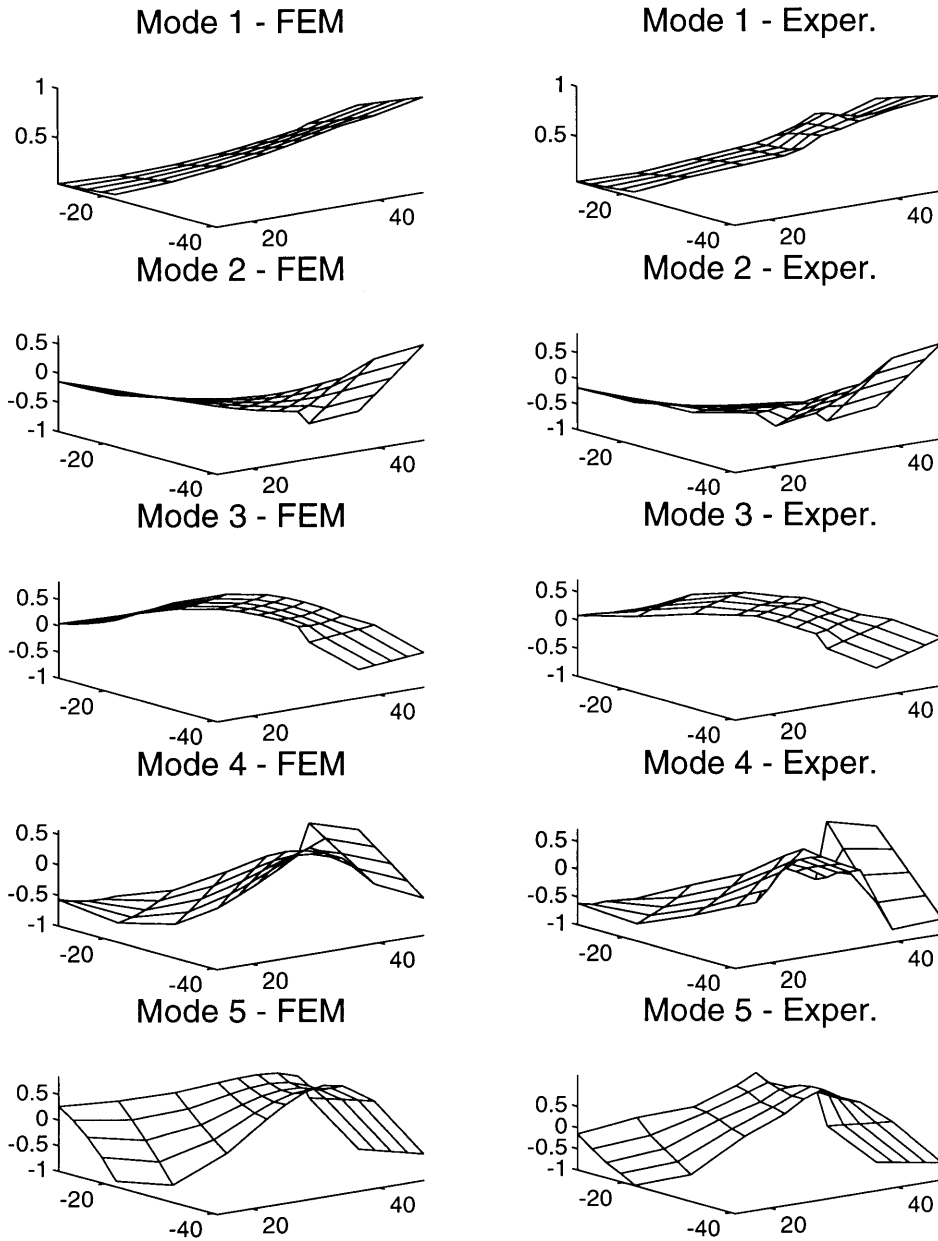
Mode 1 - FEM

Mode 1 - Exper.

Mode 2 - FEM

Mode 2 - Exper.

Mode 3 - FEM

Mode 3 - Exper.

Mode 4 - FEM

Mode 4 - Exper.

Mode 5 - FEM

Mode 5 - Exper.

Figure 4C.1: Undeployed modeshapes for the spar with the shell for experimental and finite element models (trailing edge out, root on the left)
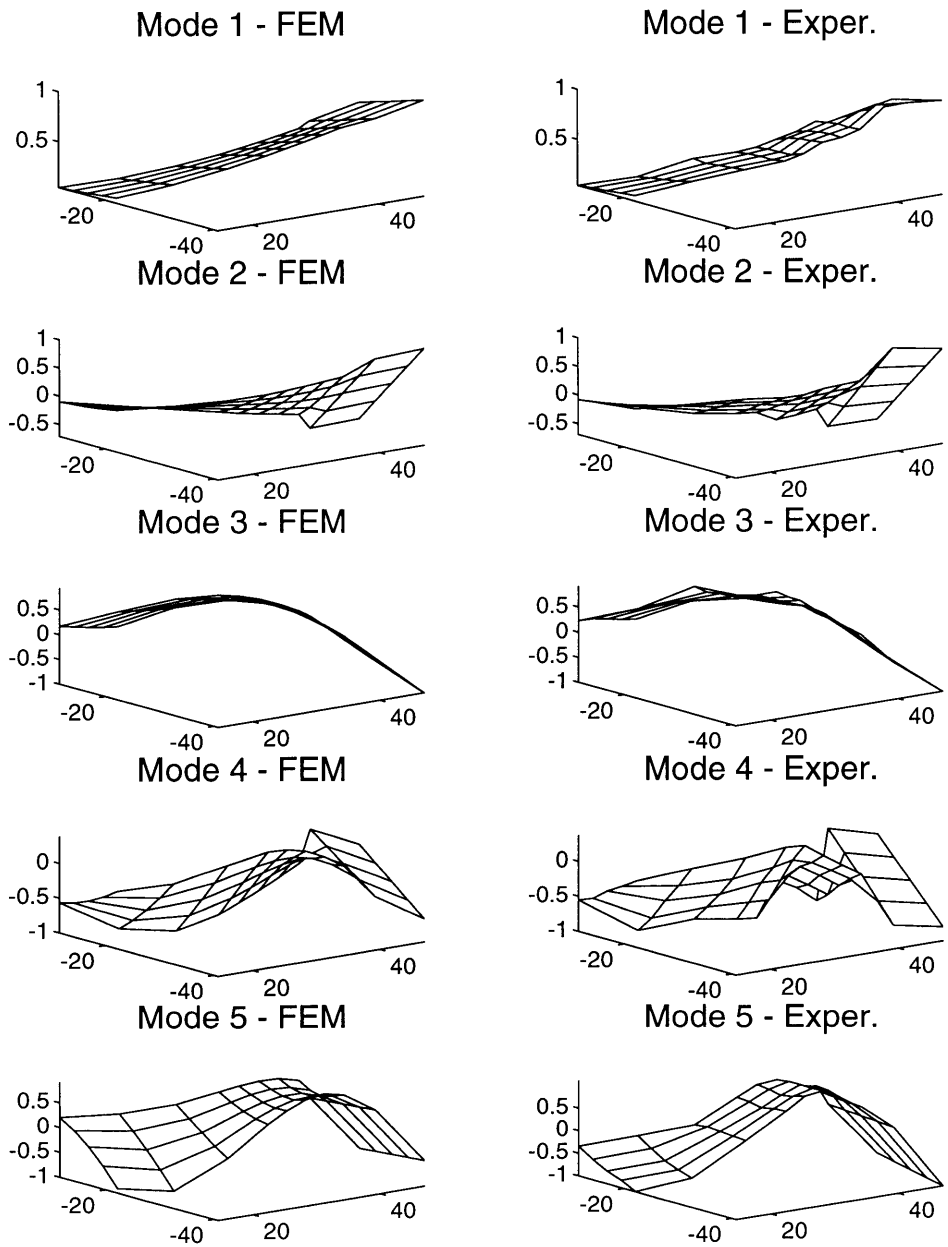
Figure 4C.2: Deployed modeshapes for the spar with the shell for experimental and finite element models (trailing edge out, root on the left)

Conclusions

Chapter 5

This thesis describes the design and modeling of an active wing for strain and flap actuated aeroelastic control. Emphasis was placed on design goals of the hardware, and experimental and analytical models were developed to evaluate the success of meeting the design targets. Experimental tests on the flutter stopper showed that the tungsten mass deployed in 0.225 seconds, and did not accidentally release when undergoing vibrations of ±3.25" in bending at 3Hz, nor at ±5° in torsion at 16 Hz. Deployment was analytically shown to raise the flutter speed by 28.2%, which is within 2% of the target value.

Using the aluminum testbench, an experimental frequency-based technique was used to create a mathematical system model, which was then compared to a finite element model. It was found that the finite element model predicted frequency reponse and modeshapes of the experimental model of testbench over the significant aeroelastic frequency bandwidth. The frequencies of the testbench model were predicted to be within 5% for the first three modes of each model configuration, and the MAC values deviated by less than 2% in the first two modes.

The identification and modeling techniques were applied to the composite spar to determine the quality of the analytical model. It was found that for a configuration without the aerodynamic shell, the FEM frequencies were within 4% of the experimental values for all of the modes under consideration in both undeployed and deployed flutter stopper cases, except for the second mode in the deployed model. The finite element model resulted in MAC values within 4% for all modes, both flutter stopper configurations, except for the fourth mode in the deployed model.

The addition of the aerodynamic shell complicated the comparison process, and considerably reduced the quality of the modeshape comparison. The inclusion of chordwise stiffeners improved the frequencies of the FE model, in particular raised the first torsional frequencies by 11.6% and 14.8% in the flutter stopper undeployed and deployed models, respectively. The finite element model frequency predictions were found to be within 3% of the experimental values for all modes except the second mode of the undeployed flutter stopper model. The MAC values were degraded by the discontinuities, as only the first two modes of the undeployed and first three modes of the deployed model had values above 0.97. However, it was determined that the finite element model preserved the general shape of the experimental modes, except for the gravity effects, which were negligible for most cases.

Appendix A: Physical Dimensions and Properties

Spar: Overall Physical Dimensions

Length	48 in. (121.9 cm)	Sweep	30° at 1/4 chord
Width	18 in. (root), 12 in. (tip)	Aspect Ratio	4 (half span)
Thickness	0.241 in (.61 cm)	Weight	11.44 lbs (5.2 kg)

Graphite/Epoxy: IM7G/3501-6 prepreg unidirectional fabric

E_L	17.8 MSI (122.8 GPa)	t_{ply}	0.006 in. (0.1524 mm)
E_T	1.20 MSI (8.30 GPa)	lay-up	$[20°_2/0°]_s$
ν	0.30 (after cure)	thickness	0.032 in. (0.813 mm)
G_{LT}	0.87 MSI (6.00 GPa)	weight	not measured
ρ	1.72×10^{-3} slug/in.^{3} (1530 kg/m^3)		

Honeycomb: 5052-H39 Hexagonal 3/16-5052-0.002

E	220 KSI (1.52 GPa)	ρ	1.02×10^{-4} slug/in.^{3} (91 kg/m^3)
G	38.5 KSI (0.62 GPa)	thickness	0.177 in. (4.488 mm)
ν	0.07	weight	not measured

Aluminum Inserts: 7075-T6

E	10.3 MSI (71.1 GPa)	thickness	0.177 in. (44.88 mm)
G	3.9 MSI (26.9 GPa)	weight	not measured
ν	0.33	dimensions	6- 1.125 x 1.125 in. (28.6 x 28.6 mm)
ρ	3.14×10^{-3} slug/in.^{3} (2795 kg/m^3)		2- 2.0 x 1.125 in. (50.8 x 28.6 mm) 1- 2.5 x 1.125 in. (63.5 x 28.6 mm) 2- 1.875 x 1.125 in. (47.6 x 28.6 mm) with 0.5 in. (12.7 mm) tabs ea. side

Steel Insert: stainless

E	29.0 MSI (200 GPa)	thickness	0.177 in. (44.88 mm)
G	11.0 MSI (75.9 GPa)	weight	not measured
ν	0.30	dimensions	l1: 18.0 in. (457.2 mm)
ρ	8.79×10^{-3} slug/in.^{3} (7823 kg/m^3)		l2: 17.192 in. (436.7 mm) w: 5.60 in. (142.24 mm)

Fiberglass: Type 120 E-Glass fabric

E	3.0 MSI (20.7 GPa)	lay-up	$[0°]_5$
G	0.8 MSI (5.5 GPa)	thickness	0.020 in. (0.508 mm)
ν	0.07	weight	not measured
t_{ply}	0.004 in. (0.102 mm)	dimensions	l1: 18.0 in. (457.2 mm)
ρ	1.15×10^{-3} slug/in.^{3} (1024 kg/m^3)		l2: 17.29 in. (439.2 mm) w: 4.75 in. (120.7 mm)

Root Attachment: 7075-T6 Aluminum

weight	8.1338 lbs (3.697 kg)	fastener weight	3.333 lbs (1.515 kg) to spar 1.657 lbs (0.753 kg) to mtg.

Mounting Assembly: 7075-T6 Aluminum

weight	54.23 lbs (24.65 kg)	fastener weight	1.569 lbs (0.713 kg)

Piezoceramic Wafer Properties: G-1195 PZT

E	8.7 MSI (60 GPa)	D_{31}	7.09×10^{-9} in/volt (180×10^{-12} m/volt)
G	3.19 MSI (22 GPa)	thickness	0.010 in. (0.254 mm)
ν	0.30	weight	6.915×10^{-3} lbs (0.0152 kg)
ρ	8.59×10^{-3} slug/in.^{3} (7650 kg/m^3)	dimensions	2 x 1.25 in. (50.8 x 25.4 mm)

Package Properties

length	4.4375 in. (112.71 mm)	thickness	0.020 in. (0.508 mm)
		weight	0.032 lbs (0.0147 kg)
width	1.4375 in. (36.5125 mm)	# / wafers	4

Flap Drive System Overall Properties

total length	41.19 in. (1046 mm)	weight	1.76 lbs (0.80 kg)

Motor and Tachometer Specifications:

torque avl.	46.875 in-lb (5.30 N-m)	weight	11.906 lbs (5.412 kg)
J (incl. tach)	7.688×10^{-3} slug-in.^{2} (72.4 kg-mm^2)	dimensions	m: 5.50 in. diam. x 2.78 in. (139.7 x 70.6 mm) t: 3.375 in. diam. x 2.19 in. (85.7 x 55.6 mm)

Graphite-Epoxy Tubes: AS4/3501-6

E	6.62 MSI (45.7 GPa)	ρ	1.72×10^{-3} slug/in.^{3} (1531 kg/m^3)
G	5.33 MSI (36.7 GPa)	lay-up	$[+45°/-45°]_r$
ν	0.30	** all values	post cure **

	J	weight	dimensions
Motor Tube	1.62×10^{-4} slug-in.^{2} (1.525 kg-mm^2)	0.11 lbs (0.05 kg)	0.65 in. OD (16.51 mm) 0.25 in. ID (6.35 mm) x 7.57 in. (192.3 mm)
Drive Tube	2.56×10^{-4} slug-in.^{2} (2.41 kg-mm^2)	0.15 lbs (0.068 kg)	0.60 in. OD (15.24 mm) 0.25 in. ID (6.35 mm) x 12.08 in. (306.83 mm)
Flap Tube	1.34×10^{-4} slug-in.^{2} (1.26 kg-mm^2)	0.108 lbs (0.0491 kg)	0.50 in. OD (12.70 mm) 0.25 in. ID (6.35 mm) x 13.46 in. (341.88 mm)

Inserts: Stainless Steel

Jtot.	1.23×10^{-4} slug-in.^{2} (1.16 kg-mm^2)	dimensions	0.25 in diam. x 1.5 in. (6.35 mm x 38.1 mm)
weight	0.2656 lbs (0.121 kg)		

Spline: GTC 12S

weight	0.309 lbs (0.1405 kg)	travel	0.25 in. (6.35 mm)
J	5.48×10^{-3} slug-in.^{2} (51.58 kg-mm^2)		

Universal Joints: Sterling Inst. S57PY5-SU0812

weight (each)	0.033 lbs (0.015 kg)	range	30°
J (each)	1.945×10^{-5} slug-in.^{2} (0.183 kg-mm^2)		

Cam: Aluminum 7075-T6

weight	0.0395 lbs (0.018 kg)	J	3.77×10^{-4} slug-in.^{2} (3.55 kg-mm^2)

Sensor: Kaman KD-2310-2UB

sensing range	0.08 in. (2.032 mm)	sensitivity	10 mV/mil
dimensions	0.40 diam. x 0.25 in. (10.2 x 6.35 mm)	weight (incl. cable)	0.106 lbs (0.0482 kg)
resolution	0.008 mil (0.203 μm)		

Sensor mount: Linear translation stage

weight	0.184 lbs (0.0836 kg)	range	0.512 in. (13 mm)
sensitivity	7.87×10^{-3} in. (2 μm)		

Flap: same materials as Shell

J (approx.)	0.01685 slug-in.^{2} (158.6 kg-mm^2)	dimensions	3.356 in. chord (85.24 mm) 8.0 in. span (203.2 mm)
		weight (with counterbalance)	0.848 lbs (0.385 kg)

Shell Overall and Sectional Properties:

weight	9.36 lbs (4.255 kg)	chord (root)	28.3 in. (718.82 mm)
span	48.4 in. (1228.7 mm)	chord (tip)	15.6 in. (396.24 mm)
t/c ratio	0.12		

	span	weight
section 1	8.15 in. (207.0 mm)	2.24 lbs (1.108 kg)
section 2	8.06 in. (204.7 mm)	2.00 lbs (0.909 kg)
section 3	8.04 in. (204.2 mm)	1.71 lbs (0.777 kg)
section 4	8.04 in. (204.2 mm)	1.23 lbs (0.559 kg)
section 5	6.49 in. (164.9 mm)	1.11 lbs (0.505 kg)
section 6	8.10 in. 205.7 mm()	1.07 lbs (0.486 kg)

Fiberglass: FIBERITE E-glass prepreg fabric

E	3.1 MSI (21.4 GPa)	t_{ply}	0.01 in. (0.254 mm)
G	1.04 MSI (7.2 GPa)	thickness	0.06 in. (1.524 mm)
ν	0.07	ρ	2.17×10 slug/in.^{3} (1931 kg/m^3)
lay-up	$[0°/90°]_3$		

Foam:

| E | 9.95 KSI (70 MPa) | ρ | 5.616×10^{-5} slug/in.^{3} |
| G | 2.99 KSI (21 MPa) | | (50 kg/m^3) |

Flutter Stopper:

| dimensions | 13.23 x 5.63 in. (336.0 x 143.0 mm) | fastener weight | 0.235 lbs (0.107 kg) |
| weight (total) | 6.438 lbs (2.926 kg) | | |

Deployable Mass: Tungsten Alloy

E	47.8 MSI (330 GPa)	ρ	0.019 slug/in^3 (17,000 kg/m^3)
G	20.3 MSI (140 GPa)	weight (including bushings and target)	3.364 lbs (1.529 kg)
ν	0.30	dimensions	4.69 x 1.4 x 1.1 in. (119.1 x 35.6 x 27.9 mm)

Rods: AISI 4130 steel

| dimensions | 0.375 diam. x 13.5 in. (9.5 x 342.9 mm) | hardness | 43-47 Rockwell (202-230 KSI τ_{su}) |
| weight (each) | 0.424 lbs (0.193 kg) | | |

Frame: Aluminum 7075-T6

| weight (total) | 0.846 lbs (0.385 kg) | dimensions | IB&OB: 12.76 x 1.0 in. (324.1 x 25.4 mm) LE&TE: 6.16 x 0.4 in. (156.5 x 10.16 mm) |

Springs: 0.029 in. steel music wire

| k | 0.265 lb/in. (0.05 N/mm) | weight (each) | 0.012 lbs (5.364×10^{-3} kg) |
| lengths: | 1.3 in. (33.0 mm) solid 11.5 in. (292.1 mm) free | dimensions | OD: 0.48 in. (12.2 mm) ID: 0.422 in. (10.7 mm) |

Electromagnet: Magnetool EMR-50

| strength | 12.5 lbs (5.682 kg) | weight | 0.1067 lbs (0.0485 kg) |
| electrical requirements | 12 V DC 1.4 W | dimensions | 0.75 in. diam. x 1.5 in. (19.05 mm x 38.1 mm) |

Position sensor and mount: push-button switch and 7075-T6

weight	0.0329 lbs (0.015 kg)

Frame attachment brackets: AISI 4140 steel

weight (each) 0.0918 lbs (0.042 kg)	dimensions	0.20 in. th. x 0.5 in. w. (5.08 x 12.7 mm)

Spar attachment brackets: 7075-T6

weight (each) 0.137 lbs (0.0623 kg)	dimensions +	4.25 x 1.75 x 0.75 in. (107.9 x 44.5 x 19.1 mm)

Shell attachment brackets: 7075-T6

weight(each) 0.078 lbs (0.0353 kg)	dimensions +	1- 2.5 x 1.0 x 0.75 in. (63.5 x 25.4 x 19.1 mm) 1- 4.0 x 1.0 x .75 in. (101.6 x 25.4 x 19.1 mm)

Latch: stainless steel

weight 0.186 lbs (0.0845 kg)	dimensions +	2.77 x 0.6 x 1.28 in. (70.4 x 15.2 x 32.5 mm)

+ Maximum dimensions

Appendix B: Aeroelastic Predictions

The aeroelastic behavior of the system is analytically predicted using an unsteady aerodynamics and aeroelastic stability package. Initially, a simple extrapolation of the modeshapes is used to include points along the leading and trailing edges of the shell. The modified finite element model is then input into the unsteady aerodynamic code UNSAER to determine the generalized aerodynamic coefficients over the structure for given values of reduced frequency for the first four modes of the system. The aerodynamic data is input to the stability code ASAN to determine the stability parameters and flutter behavior of the system, given the dynamic structural model of the system. The result of this analysis is that the undeployed flutter stopper model flutters at 267 ft/sec (81 m/sec) and the deployed model flutters at 333 ft/sec (102 m/sec), which means that the deployment of the flutter stopper causes an increase of 26% in flight speed. Both flutter mechanisms are a coalescence of the first and second modes, as designed. Note that the mode which actually becomes unstable is different between the two models, which indicates that there is a more fundamental difference between the two physical models than just the shift in CG. The following pages contain the results of these analyses, in the form of two tables of frequencies and damping ratios at selected flight speeds, and plots of frequency and damping ratio versus flight speed for both flutter stopper configurations.

Table B.1: Frequency and damping ratios of the undeployed flutter stopper
model at selected airspeeds from analytical flutter predictions

ft/sec	Mode 1: Freq. (Hz)	Mode 1: % Damp.	Mode 2: Freq. (Hz)	Mode 2: % Damp.	Mode 3: Freq. (Hz)	Mode 3: % Damp.	Mode 4: Freq. (Hz)	Mode 4: % Damp.
0.0	2.445	1.002	12.460	1.000	17.317	1.000	35.579	1.000
41.7	2.477	3.187	12.325	1.289	17.152	1.990	35.294	1.228
83.3	2.614	5.286	12.093	1.771	17.185	2.894	35.142	1.303
125.0	2.860	7.271	11.662	2.434	17.259	3.756	34.965	1.435
166.7	3.250	9.176	11.033	3.319	17.302	4.569	34.650	1.575
208.3	3.872	11.144	10.110	4.270	17.364	5.343	34.279	1.698
250.0	5.048	14.226	8.578	4.343	17.439	6.099	33.831	1.787
267.1 **	6.068	21.640	7.437	-0.254	17.472	6.409	33.600	1.807
291.7	6.385	41.889	6.763	-20.734	17.522	6.863	33.240	1.820
333.3	6.266	58.897	6.387	-40.891	17.582	7.665	32.559	1.782

Table B.2: Frequency and damping ratios of the deployed flutter stopper
model at selected airspeeds from analytical flutter predictions

| ft/sec	Mode 1: Freq. (Hz)	Mode 1: % Damp.	Mode 2: Freq. (Hz)	Mode 2: % Damp.	Mode 3: Freq. (Hz)	Mode 3: % Damp.	Mode 4: Freq. (Hz)	Mode 4: % Damp.
0	2.639	1.001	11.878	1.000	17.141	1.000	35.739	1.000
41.7	2.663	3.251	11.796	1.917	16.942	1.797	35.456	1.238
83.3	2.783	5.381	11.686	2.935	16.964	2.528	35.311	1.363
125.0	2.989	7.275	11.481	4.081	17.023	3.272	35.125	1.528
166.7	3.293	8.880	11.198	5.434	17.041	3.990	34.798	1.707
208.3	3.722	10.142	10.813	7.024	17.078	4.676	34.411	1.871
250.0	4.328	10.956	10.266	8.990	17.126	5.322	33.943	2.008
291.7	5.250	10.864	9.451	11.92	17.177	5.923	33.329	2.096
333.3 **	6.964	-0.548	7.969	24.828	17.178	5.448	32.620	2.124
375.0	7.212	-20.458	7.975	42.692	17.130	6.868	31.816	2.067
416.7	7.335	-31.628	8.233	52.122	17.031	7.130	30.919	1.899
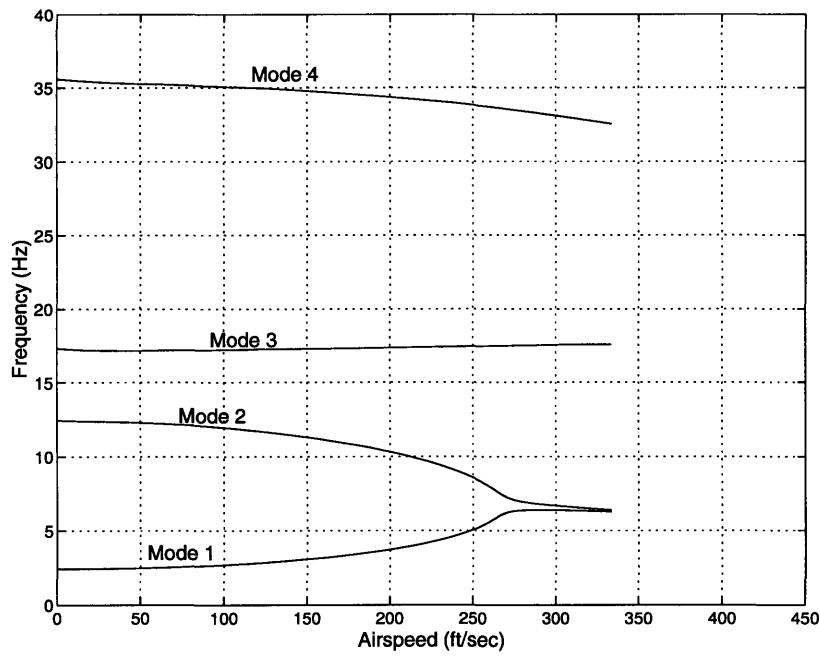
Figure B.1: Natural frequency versus airspeed for the first four modes of the flutter stopper undeployed model
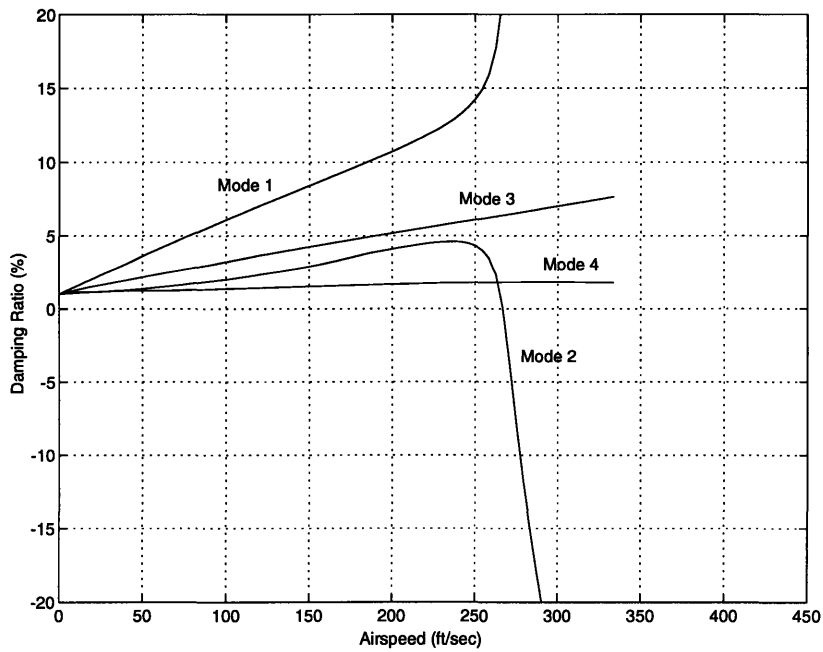

Figure B.2: Damping ratio versus airspeed for the first four modes of the flutter stopper undeployed configuration
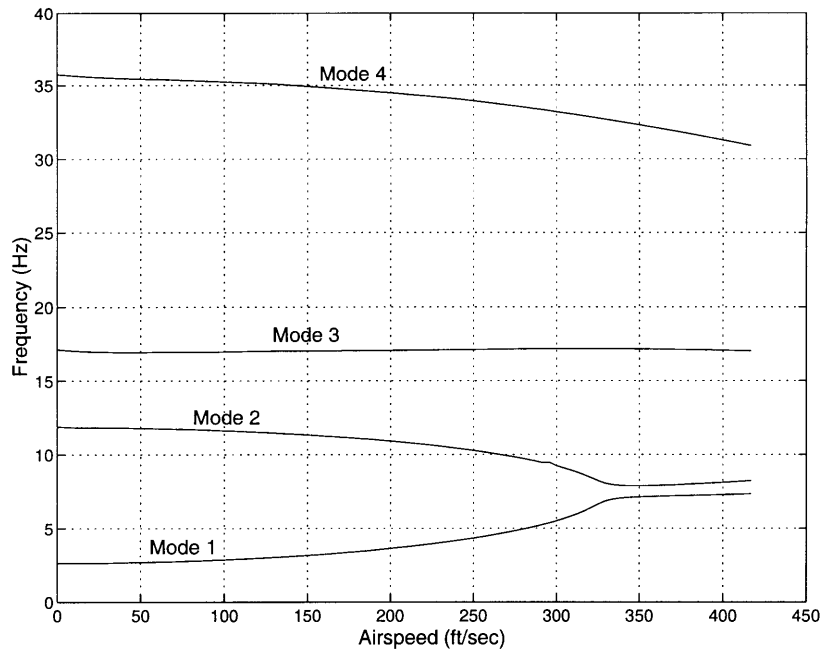
87

Figure B.3: Natural frequency versus airspeed for the first four modes of the flutter stopper deployed configuration
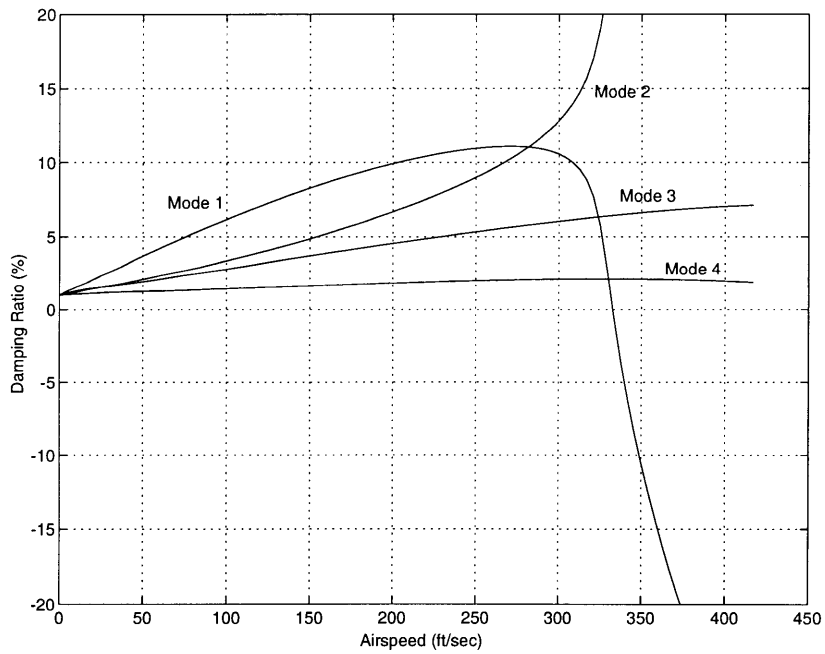

Figure B.4: Damping ratio versus airspeed for the first four modes of the flutter stopper deployed configuration

88

Bibliography

Balmes, E., and Crawley, E.F., 1993. "Experimental/Analytical Predictive Models of Damped Structural Dynamics," SERC Report #7-93, Massachusetts Institute of Technology, Cambridge, MA.

Bisplinghoff, R.L., Ashley, H., and Halfman, R.L., 1955. *Aeroelasticity*. Reading, Massachusetts: Addison-Wesley Publishing Company.

Blevins, R.D., 1984. *Formulas for Natural Frequency and Mode Shape*. Malabar, Florida: Robert E. Krieger Publishing Company.

Cook, R.D., Malkus, D.S., and Plesha, M.E., 1989. *Concepts and Applications of Finite Element Analysis*. New York: John Wiley and Sons.

Crawley, E.F., and Lazarus, K.B., 1991. "Induced Strain Actuation of Isotropic and Anisotropic Plates," *AIAA Journal*, Vol. 29, No. 6, pp. 944-951.

Ehlers, S.M., and Weisshaar, T.A., 1990. "Static Aeroelastic Behavior of an Adaptive Laminated Piezoelectric Composite Wing," AIAA Paper No. 90-1078, *Proceedings of the 31st Structures, Structural Dynamics, and Materials Conference*, Long Beach, CA, pp. 1611-1623.

Ewins, D.J., 1984. *Modal Testing: Theory and Practice*. New York: John Wiley and Sons.

Heeg, J., 1992. "An Analytical and Experimental Investigation of Flutter Suppression via Piezoelectric Actuation," AIAA Paper No. 92-2106, *Proceedings of the AIAA Dynamics Specialists Conference*, Dallas, TX, pp. 237-247.

Hollowell, S.J., and Dugundji, J., 1984. "Aeroelastic Flutter and Divergence of Stiffness Coupled, Graphite/Epoxy, Cantilevered Plates," *Journal of Aircraft*, Vol. 21, No. 1, pp. 69-76.

Hwang, C. et al, 1980. Wind Tunnel Test of a Fighter Aircraft Wing/Store Flutter Suppression System - An International Effort," AGARD R-689.

Jacques, R.N., and Miller, D.W., 1993. "Multivariable Model Identification from Frequency Response Data," *Proceedings of the 32nd Conference on Decision and Control*.

Jensen, D.W., and Crawley, E.F., 1984. "Frequency Determination Techniques for Cantilevered Plates with Bending-Torsion Coupling," *AIAA Journal*, Vol. 22, No. 3, pp. 415-420.

Jones, R.M., 1975. *Mechanics of Composite Materials*. New York: Hemisphere Publishing Corporation,.

Kuethe, A.M., and Chow, C.Y., 1986. *Foundations of Aerodynamics: Bases of Aerodynamic Design*. New York: John Wiley and Sons.

Landsberger, B.J., and Dugundji, J., 1985. "Experimental Aeroelastic Behavior of Unswept and Forward-Swept Cantilever Graphite/Epoxy Wings," *Journal of Aircraft*, Vol. 22, No. 8, pp. 679-686.

Lazarus, K.B., and Crawley, E.F., 1989. "Induced Strain Actuation of Composite Plates," GTL Report #197, Massachusetts Institute of Technology, Cambridge, MA.

Lazarus, K.B., and Crawley, E.F., 1992. "Multivariable High-Authority Control of Plate-Like Active Lifting Surfaces," SERC Report #14-92, Massachusetts Institute of Technology, Cambridge, MA.

Lin, C.Y., and Crawley, E.F, 1993. "Strain Actuated Aeroelastic Control," SERC Report #2-93, Massachusetts Institute of Technology, Cambridge, MA.

Meirovitch, L., 1980. *Elements of Vibration Analysis*. New York: McGraw-Hill Book Company.

Newsom, J.R., Pototsky, A.S., and Abel, I., 1985. "Design of a Flutter Suppression System for an Experimental Drone Aircraft," *Journal of Aircraft*, Vol. 22, No. 5, pp. 380-386.

Noll, T., et al, 1989. "Aeroservoelastic Wind-Tunnel Investigations Using The Active Flexible Wing Model - Status and Recent Accomplishments," NASA CP-1168.

Pendleton, E., Lee, M., and Wasserman, L., 1992. "Application of Active Flexible Wing Technology to the Agile Falcon," *Journal of Aircraft*, Vol. 29, No. 3, pp. 444-451.

Perry, B. III, et al, 1990. "Digital-Flutter-Suppression-System Investigations for the Active Flexible Wing Wind-Tunnel Model," AIAA Paper No, 90-1074, *Proceedings of the 31st Structures, Structural Dynamics, and Materials Conference*, Long Beach, CA, pp. 1571-1581.

Ricketts, R.H., and Doggett, R.V. Jr., 1980. "Wind-Tunnel Experiments on Divergence of Forward-Swept Wings," NASA TP-1685.

Reed, W.H. III, Foughner, J.T. Jr., and Runyan, H.L. Jr., 1980. "Decoupler Pylon: A Simple, Effective Wing/Store Flutter Suppressor,", Journal of Aircraft, Vol. 17, No. 3, pp. 206-211.

Strang, G., 1986. *Introduction to Applied Mathematics*. Wellesley, Massachusetts: Wellesley-Cambridge Press.

Suh, N.P., 1990. *The Principles of Design*. New York: Oxford University Press.

Turner, M.R., 1975. "Active Flutter Suppression," AGARD CP-175.